JGR Atmospheres

RESEARCH ARTICLE
10.1029/2021JD035907

Melting Behavior of Rimed and Unrimed Snowflakes Investigated With Statistics of Triple-Frequency Doppler Radar Observations

Markus Karrer[1], José Dias Neto[1,2], Leonie von Terzi[1], and Stefan Kneifel[1]

[1]Institute for Geophysics and Meteorology, University of Cologne, Köln, Germany, [2]Department of Geosciences and Remote Sensing, Delft University of Technology, Delft, The Netherlands

Key Points:

- We investigated the growth or shrinking of snowflakes in the melting layer using statistics of multi-frequency Doppler radar observations
- Reflectivity flux analysis indicates only slight differences for unrimed or rimed particles
- Growth or shrinking processes either compensate each other or have, on average, only a small impact on the reflectivity flux

Correspondence to:
S. Kneifel,
skneifel@meteo.uni-koeln.de

Citation:
Karrer, M., Dias Neto, J., von Terzi, L., & Kneifel, S. (2022). Melting behavior of rimed and unrimed snowflakes investigated with statistics of Triple-frequency Doppler radar observations. *Journal of Geophysical Research: Atmospheres*, *127*, e2021JD035907. https://doi.org/10.1029/2021JD035907

Received 28 SEP 2021
Accepted 16 MAR 2022

Author Contributions:
Conceptualization: Stefan Kneifel
Data curation: Leonie von Terzi
Formal analysis: Markus Karrer, José Dias Neto
Funding acquisition: Stefan Kneifel
Investigation: Markus Karrer, José Dias Neto
Methodology: Markus Karrer, José Dias Neto, Leonie von Terzi
Project Administration: Stefan Kneifel
Software: Markus Karrer, José Dias Neto, Leonie von Terzi
Supervision: Stefan Kneifel
Visualization: Markus Karrer
Writing – original draft: Markus Karrer
Writing – review & editing: Markus Karrer, Stefan Kneifel

Abstract Comparing the reflectivity flux at the top and bottom of the melting layer (ML) reveals the overall effect of the microphysical processes occurring within the ML on the particle population. If melting is the only process taking place and all particles scatter in the Rayleigh regime, the reflectivity flux increases in the ML by a constant factor given by the ratio of the dielectric factors. Deviations from this constant factor can indicate that either growth or shrinking processes (breakup, sublimation, and evaporation) dominate. However, inference of growth or shrinking dominance from the increase in reflectivity flux is only possible if other influences (e.g., vertical wind speed) are negligible or corrected. By analyzing radar Doppler spectra and multi-frequency observations, we correct the reflectivity fluxes for vertical wind and categorize the height profiles by the riming degree at the ML top. We apply this reflectivity flux ratio (ZFR) approach to a multi-month mid-latitude winter data set that contains mostly stratiform clouds. The profiles of radar variables in the ML are found to be surprisingly similar for both unrimed and rimed profiles with slight differences, for example, in the absolute values of the reflectivity flux. Statistical analysis of the ZFR suggests that either microphysical processes other than melting are not important or strongly compensate for each other. The results seem to confirm that at least for moderately precipitating stratiform clouds, the melting-only assumption applied in several retrievals and microphysical schemes is reasonable.

Plain Language Summary To better predict precipitation by numerical models and quantify precipitation by observations, it is important to improve the understanding of processes in the melting layer (ML). The ML is the part of clouds where ice particles melt and become rain. We use an approach that assesses whether a tendency toward either growth or shrinking processes is evident in the ML. We assess the uncertainty of the approach, correct for different factors, and apply it to a large data set to derive robust statistics separately for profiles with different characteristic ice particle shapes above the ML. These statistics are surprisingly similar for the different characteristic ice particle shapes and suggest that either growth and shrinking processes are not important in the ML or strongly compensate for each other.

1. Introduction

More than 70% of rainfall reaching the Earth's surface is generated in the ice phase (Heymsfield et al., 2020). After nucleation, ice particles can grow by a complex interplay of microphysical processes such as vapor deposition, aggregation, and riming. Once these particles sediment down to a temperature of 0°C, they start to melt into raindrops. The transition layer, where partially melted ice particles and raindrops coexist, is commonly called the melting layer (ML).

Most prominently, the ML can be detected in radar observations. The big difference of the refractive index of ice and liquid water in the microwave and the higher fall velocity of liquid particles are mainly responsible for the well-known radar bright band, that is, a region of strongly enhanced radar reflectivity (Fabry, 2015). In addition, polarimetric observations and signal attenuation are affected by the ML (Ryzhkov & Zrnic, 2019). To avoid biases in surface precipitation estimates, one must carefully consider these ML effects. Specifically for space-borne retrievals based on observations from higher frequency radars (Ka- or W-band), the attenuation effect of the ML is considered explicitly by a ML model (Kidd et al., 2020).

The characterization of the morphological changes during the melting of individual ice particles is only one important scientific problem that hampers a more accurate characterization of the particle's scattering properties

and the development of improved microphysical parametrizations of melting. The melting of sedimenting ice particles does not happen instantaneously but depends on the temperature and humidity of the surrounding air (Heymsfield et al., 2021; Matsuo & Sasyo, 1981a, 1981b; Matsuo et al., 1981; Mitra et al., 1990). In addition, the evolution of melting also depends on the properties of the ice particles themselves, such as size, density, and fall velocity (Pruppacher et al., 1998). As a result, the ML can often have a vertical extent of a few hundred meters. Because of this large vertical extent, various microphysical processes (e.g., particle breakup) that are currently poorly understood can substantially influence the hydrometeor population.

Primarily in situ observations have been used to infer the presence and relevance of different processes in the ML (Barthazy et al., 1998; Heymsfield et al., 2015; Stewart et al., 1984; Willis & Heymsfield, 1989). Depositional growth and condensation are relatively slow growth processes compared to aggregation or riming at temperatures slightly below 0°C and therefore also within the ML (Heymsfield et al., 2015). Evidence for additional aggregation within the ML has been found in several studies (Barthazy et al., 1998; Heymsfield et al., 2015; McFarquhar, 2004; Stewart et al., 1984; Willis & Heymsfield, 1989; Yokoyama et al., 1985). In particular, the larger aggregates entering the ML can be expected to further aggregate due to increasing differential sedimentation velocities, enhanced sticking efficiency, and the longer time large aggregates need to melt (e.g., Willis & Heymsfield, 1989). In addition to aggregation, the mass of large snowflakes might also increase by accretion (collection of liquid droplets by melting particles), including capturing small drops originating from already melted small ice particles. Once completely melted, the resulting raindrop might not be aerodynamically stable, and drop breakup can occur for particles larger than about 5 mm (Pruppacher et al., 1998).

Besides processes affecting pure ice-phase (aggregation, accretion, and fragmentation) and pure liquid phase particles (e.g., collision-coalescence and hydrodynamic breakup), also partially melted particles might collide or fragment. Laboratory studies found that when large graupel or hail particles (larger than about 9 mm) melt, a water torus surrounds the particle and eventually drops shed from it (Pruppacher et al., 1998; Rasmussen & Heymsfield, 1987). Breakup of smaller particles, which is usually referred to as melting fragmentation, were observed in laboratory (Knight, 1979; Mitra et al., 1990; Oraltay & Hallett, 1989, 2005) and also found in 3D melting particle simulations (Leinonen & von Lerber, 2018). However, Oraltay and Hallett (1989) observed melting fragmentation only for relative humidities below 70% with reference to liquid water and certain ice particle habits such as dendrites. However, the description remains qualitative, and parametrization for the frequency of fragments produced by melting fragmentation does not exist.

Even more uncertain than the specific processes is their relative importance. In situ studies such as Yokoyama et al. (1985) and Barthazy et al. (1998) suggested that aggregation in the upper part of the ML (close to the maximum of reflectivity) is in balance with breakup below. However, studies comparing observed and simulated reflectivity (Ze) and mean Doppler velocity (MDV) profiles within the ML revealed that aggregation and breakup are not essential to explain the typical radar reflectivity profile within the ML but might still occur (Fabry & Zawadzki, 1995; Klaassen, 1988).

How much these processes might alter the particle population properties in the ML is particularly relevant because many microphysical schemes (Morrison et al., 2009; Seifert & Beheng, 2006; Thompson et al., 2008) and retrievals (Kidd et al., 2020) treat melting in a rather simplistic way. In these schemes melting converts particles mass (and number in the case of two-moment schemes) directly from the ice-to the liquid-phase particle category and assume that the mean mass (total mass of particle population divided by total number) is conserved during this conversion. Although the microphysical schemes allow aggregation to continue in the ML, its effect might be underestimated because the depth of the ML is often underestimated (e.g., Frick et al., 2013). Microphysical schemes with an explicit treatment of the shapes of the melting particles (Brdar & Seifert, 2018; Cholette et al., 2019; Frick et al., 2013; Phillips et al., 2007; Szyrmer & Zawadzki, 1999; Thériault & Stewart, 2010) can more accurately simulate processes within the ML and even consider the shedding process (Rasmussen & Heymsfield, 1987). These schemes allow a more accurate simulation of ML depth, latent heat exchange, and phase (snow or rain) of the precipitation. However, an important issue for further developing those detailed models is our lack of physical understanding of certain processes. As mentioned before, one example is melting fragmentation. Analysis of in situ and remote sensing observations can provide indications of which processes are most likely to explain discrepancies between model simulations and observations (Bringi et al., 2020). Such results can then guide laboratory studies to further investigate and refine specific processes as a basis for improved model parametrizations.

Although the ML is a prominent feature in radar observations, its interpretation in terms of microphysical processes is very complicated. First, the scattering properties of the particles change drastically, as not only the shape and size of the ice particles change but also their refractive index. Second, the simultaneous occurrence of several microphysical processes in the ML makes identification or even quantification of specific processes extremely challenging. Drummond et al. (1996) presented an approach that avoids interpreting the radar signals inside the ML but instead intends to infer dominant processes by comparing the reflectivity flux

$$F_Z\left[mm^6m^{-2}s^{-1}\right] = Ze\left[mm^6m^{-3}\right] \cdot MDV\left[ms^{-1}\right] \tag{1}$$

between the top and the bottom of the ML. A specific ratio of the fluxes can be expected under the assumption of steady-state conditions and a scenario of every snowflake melting into a single drop ("melting-only" assumption). Observed deviations from this ratio are often interpreted as additional growth or shrinking (aggregation, breakup, sublimation, and evaporation) processes within the ML. The presence of such processes implies a change in mean mass or even mass flux, which is not considered in many microphysical models, or precipitation retrievals. Deviations from the constant ratio could also be caused by vertical wind, inhomogeneities, and the generation of new particles (e.g., raindrops). Two recent studies found that the reflectivity flux ratio (ZFR) is in general close to the melting-only scenario but also observed dependencies of this ratio on the ML depth (Gatlin et al., 2018) and particle type (unrimed or rimed) on top of the ML (Mróz et al., 2021).

This study investigates the validity of the melting-only scenario based on a multi-month radar data set obtained at a mid-latitude site. Previous studies revealed that ML characteristics and processes inside the ML might depend on the properties of the ice and snow particles entering the ML. For example, the observed sagging of the ML has been explained by either especially dense particles (due to riming) on top of the ML (Kumjian et al., 2016) or by intense precipitation (Li et al., 2020). Multi-frequency and Doppler radars are especially helpful to detect particle populations grown preferentially by aggregation or riming and have been used previously, for example, by Li et al. (2020), to categorize the particle type on top of the ML. Using a revisited ZFR approach from Drummond et al. (1996) combined with multi-frequency and Doppler spectral methods, we characterize mean properties of our data set in height profiles (Section 5) and investigate whether the melting-only assumption is a good approximation for the different particle types (Section 6).

The revisited ZFR approach from Drummond et al. (1996) is elaborated in detail in Section 2 and applied to a multi-month data set in Section 3. Multi-frequency and Doppler spectral techniques are used to categorize the particles by their degree of riming at the ML top and estimate the impact of vertical wind on ZFRs (Section 4). After the discussion of mean profiles within the ML (Section 5), the results of ZFR statistics for unrimed, transitional, and rimed particle categories are presented in Section 6. Section 7 provides conclusions and outlook.

2. Theoretical Background: Reflectivity Flux Ratio (ZFR) Approach

In contrast to regions above the ML, where the growth processes manifest themselves clearly in an increase in Ze, the gradient of Ze cannot be used as an indicator of particle growth or shrinking within the ML (Figure 1a). Ze is defined as

$$Ze\left[mm^6m^{-3}\right] = \frac{\lambda^4}{|K_w|^2\pi^5}\eta \tag{2}$$

where λ is the radar wavelength, and K_w the Clausius-Mossotti factor (also commonly called dielectric factor)

$$K = \frac{m_{refr}^2 - 1}{m_{refr}^2 + 1} \tag{3}$$

of liquid water. m_{refr} is the complex refractive index, which depends on the material (ice or liquid water), wavelength and temperature. η is the volume-averaged backscattering cross-section (also called reflectivity):

$$\eta = \int_0^\infty N(m)\sigma_b(m)dm \tag{4}$$

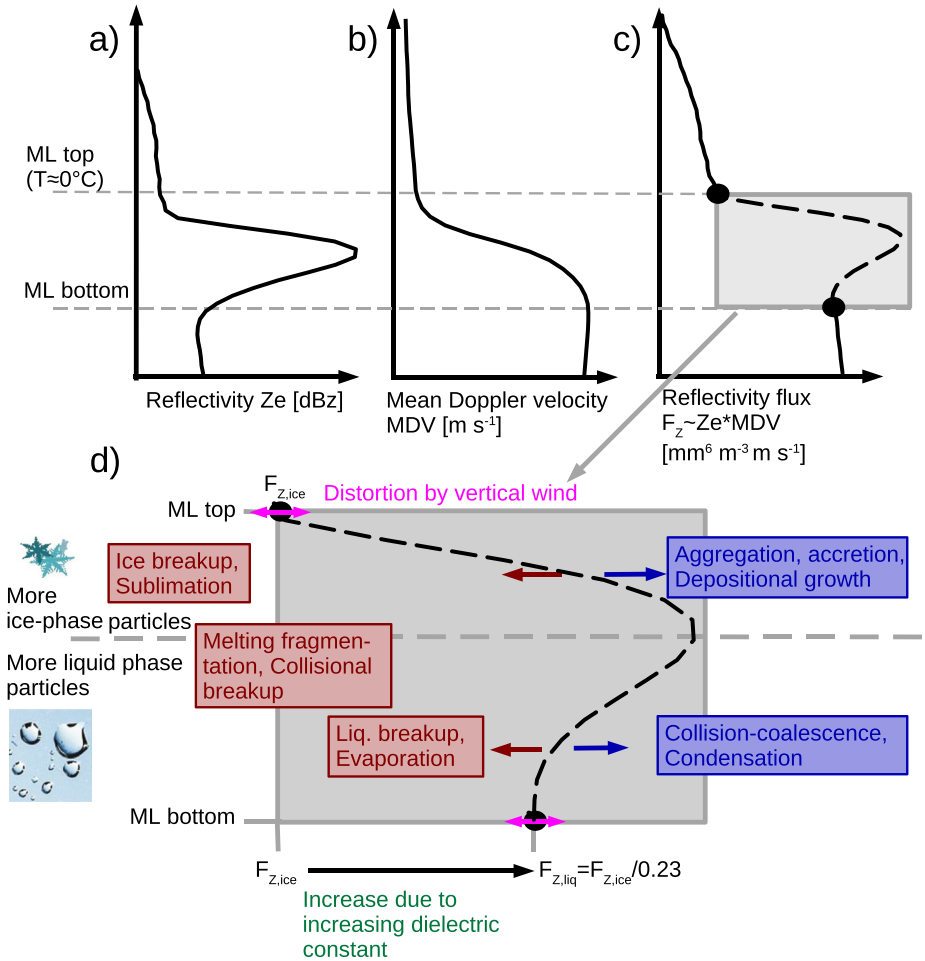

Figure 1. Schematic of radar profiles, which motivates the use of the reflectivity flux F_Z to diagnose the dominance of growth or shrinking processes within the melting layer. Panels (a–c) show typical profiles of reflectivity (a), mean Doppler velocity (b) and F_Z (c) through the ML. Panel (d) summarizes the most relevant microphysical processes inside the ML and their influence on F_Z.

$N(m)$ is the number of particles of mass m per unit volume, and $\sigma_b(m)$ is the single-particle backscattering cross-section.

Near the ML top, ice particles typically have a low density and thus have a much larger maximum dimension than a raindrop of the same mass. Once these ice particles start to melt and become wet, they backscatter more power than the dry ice particle because $|K|^2$ is about five times higher for liquid ($|K_w|^2 = 0.93$) than for ice ($|K_i|^2 = 0.18$) at a frequency of 9.6 GHz and 0°C (e.g., Ori & Kneifel, 2018). Simply put, radars see these ice particles roughly like raindrops with a large maximum dimension. One can assign the maximum of Ze (the bright band) to the height, where the particles still have a low density and therefore fall relatively slow, but contain already some liquid water. Lower down in the ML, the particles' shapes collapse, and their maximum dimensions decrease leading to an increasing velocity. As a result of this increase in velocity and the resulting divergence, the number concentration $N = \int_0^\infty N(D)dD$ decreases. This decrease in N finally also reduces Ze (Figures 1a and 1b).

Drummond et al. (1996) proposed that in stationary conditions if each snowflake melts into a raindrop of the same mass (melting-only assumption), then F_Z increases by a constant factor in the ML. In the following, we first describe why F_Z (and other fluxes) increases by a constant factor under the melting-only assumption and which additional conditions must be met when this concept is applied to radar data. Furthermore, we derive the factor by which F_Z increases through the whole ML in this case.

Under the melting-only assumption, the product of number concentration N and velocity v for a given mass m is conserved through the ML (Equation 2 in Drummond et al. (1996)):

$$N_{snow}(m)v_{snow}(m) = N_{rain}(m)v_{rain}(m) \tag{5}$$

Equation 5 can also be interpreted as follows: the number of particles that enter the ML during a certain time period Δt equals the number of particles exiting the ML through an area of the same size and for the same time interval. Equation 5 is strictly speaking only valid if the same population of particles is followed. However, a vertically pointing radar does usually not observe particle trajectories. Particles, for example, observed while entering the ML at one particular time will be advected out of the radar beam before they reach the ML bottom. Hence, we implicitly assume homogeneous conditions for applying Equation 5 using vertically pointing observations. During the time it usually takes a particle to pass through the ML, the properties of the ice particle population entering the ML must be relatively constant. Taking into account Equation 5 and the conservation of single particle masses ($m_{snow} = m_{rain}$), which is given by the melting-only assumption, it follows that the fluxes $F^{(n)}$ of any nth moment

$$F^{(n)} = \int_0^\infty N_{snow}(m)v_{snow}(m)m^n dm = \int_0^\infty N_{rain}(m)v_{rain}(m)m^n dm \tag{6}$$

are conserved, including the number flux $F_N = F^{(0)}$, mass flux $F_m = F^{(1)}$ (i.e., precipitation rate) and equivalent reflectivity flux $F_{Ze} = F^{(2)}$. The conservation of F_{Ze} is particularly interesting because it is strongly connected to F_Z. To illustrate this connection, we decompose F_{Ze} into the product of the nth moment $M^{(n)}$ of the mass distribution:

$$M^{(n)} = \int_0^\infty N(m)m^n dm \tag{7}$$

and the m^n-weighted fall velocity $v^{(n)}$:

$$v^{(n)} = \frac{1}{M^{(n)}} \int_0^\infty N(m)v(m)m^n dm \tag{8}$$

which gives:

$$F^{(n)} = M^{(n)}_{snow}v^{(n)}_{snow} = M^{(n)}_{rain}v^{(n)}_{rain} \tag{9}$$

If all raindrops are much smaller than the wavelength, the Rayleigh approximation is valid and $\sigma_{b,r}$ can be given as

$$\sigma_{b,r} = \frac{\pi^5|K_w|^2}{\lambda^4} D^6_{eq,r} = \frac{\pi^5|K_w|^2}{\lambda^4}\left(\frac{6}{\pi\rho_{liq}}\right)^2 m_r^2 \tag{10}$$

where $D_{eq,r}$ is the mass-equivalent diameter of the raindrop, $\rho_{liq} = 10^3$ kg m^{-3} the density of water, and m_r the mass of the raindrop. Combining Equations 4 and 10 one can easily see that η and thus Ze is proportional to $M^{(2)}$. Out of the same considerations, we see that MDV is the m^2 weighted velocity ($v^{(2)}$) and thus F_Z is proportional to F_{Ze}. Also for complex shaped ice particles, which are small compared to the wavelength, σ_b can be well approximated by σ_b of a solid sphere with the same mass as the complex shaped ice particles (Matrosov, 2007):

$$\sigma_{b,i} = \frac{\pi^5|K_i|^2}{\lambda^4} D^6_{eq,i} = \frac{\pi^5|K_i|^2}{\lambda^4}\left(\frac{6}{\pi\rho_{ice}}\right)^2 m_i^2 \tag{11}$$

where $D_{eq,i}$ is the mass-equivalent diameter of the ice particle, $\rho_{ice} = 917$ kg m^{-3} the density of ice and m_i the mass of the ice particle. Deviations of $|K_i|$ should be considered if the monomers composing the snow particles are nonspherical (Hogan et al., 2017).

Comparing Equations 10 and 11 tells us that a raindrop of the same mass as an ice particle ($m_r = m_i$) has a 4.38 higher σ_b:

$$\frac{\sigma_{b,r}}{\sigma_{b,i}} = \frac{|K_w|^2\rho_{ice}^2}{|K_i|^2\rho_{liq}^2} = 4.38 \tag{12}$$

As a result, F_Z is 4.38 times larger in rain than in ice if the melting-only conditions are met. Considering additionally that MDV is the sum of $v^{(2)}$ and the vertical wind w, we can define the ZFR:

$$ZFR = log_{10}\left(0.23\frac{Ze_{rain}\,(MDV_{rain} - w_{bottom})}{Ze_{snow}\,(MDV_{snow} - w_{top})}\right), \tag{13}$$

which indicates the dominance of growth mechanisms for values above zero and shrinking mechanisms for values below zero. In Equation 13, w_{top} (w_{bottom}) is the vertical wind at the ML top (bottom). Deviations from the melting-only assumption can either result from a change in the mass (F_m) or number flux (F_n). If F_m is unchanged within the ML (no deposition, sublimation, condensation, and evaporation), then ZFR indicates directly whether collisions (ZFR > 0) or breakup processes (ZFR < 0) are dominant. When ZFR is close to zero, either no process is strong enough to cause substantial changes in F_Z, or two or more processes (e.g., aggregation and breakup) compensate each other.

Within the ML, the particle population can contain pure liquid phase, melting, and pure ice phase particles. Thus, many processes could be relevant and cause deviations from the melting-only assumption (ZFR = 0). To simplify the discussion, we separated the ML using the maximum of F_Z into an upper part where ice-phase particles (or particles in the initial melting stage) are dominant and a lower part where liquid-phase particles (or almost melted particles) are dominant (Figure 1d). Furthermore, we use the terminology of pure ice-phase and pure liquid-phase microphysical processes near the ML boundaries. Predominantly ice-phase particle populations can shrink due to ice breakup and sublimation and grow due to aggregation, accretion, and depositional growth. Predominantly liquid-phase particle populations can shrink due to liquid breakup and evaporation and grow due to collision-coalescence, and condensation (Pruppacher et al., 1998). In the center of the ML, breakup due to melting fragmentation or as a result of collisions of melting particles might also be relevant.

3. Data Set

For this study, we analyze vertically pointing multi-frequency and Doppler spectral information obtained during the "TRIple-frequency and Polarimetric radar Experiment for improving process observation of winter precipitation" (TRIPEx-pol) campaign. TRIPEx-pol took place at Jülich Observatory for Cloud Evolution Core Facility, Germany (JOYCE-CF; Löhnert et al., 2015) from 11 November 2018 to 21 February 2019 (von Terzi, 2021). In total this data set includes 132 hr of ML observations.

The data quality control and post-processing of the TRIPEx-pol data set have been performed analogously to a previous multi-frequency campaign data set described in detail in Neto et al. (2019). The main difference in terms of instrumentation, is a new vertically pointing X-band Doppler radar providing higher sensitivity and Doppler spectra. In order to limit radar volume mismatching, the three radars are installed on the same roof platform in less than 10 m horizontal distance. Also, the temporal averaging and range gate resolution is very closely matched, as summarized in Table 1.

The absolute calibration of Ze for all three radars has been evaluated using raindrop size distributions from several rain events measured by a Parsivel disdrometer (Löffler-Mang & Joss, 2000) installed directly next to the radars. As demonstrated with the TRIPEx-pol data set in Myagkov et al. (2020), using rain as a calibration target provides similar accuracy (±0.7 dB) as compared to more comprehensive calibration methods. Differential attenuation has been mitigated in several steps. First, the temperature and humidity information from the European Centre for Medium-Range Weather Forecasts Integrated Forecast System (ECMWF-IFS) included in the Cloudnet products for JOYCE-CF (Illingworth et al., 2007) have been used to correct for gas attenuation (Neto et al., 2019). The remaining path integrated differential attenuation due to rain, ML and snow was estimated at cloud top with a reflectivity threshold method as described, for example, in Tridon et al. (2020). The estimated total differential attenuation is then applied to the entire Ze profile. Estimating differential attenuation is crucial for accurate derivation of the dual-wavelength ratio used in the categorizing of the profiles by their degree of riming (Section 4.4). The correction for the attenuation caused by melting particles, which was not applied in the initial data set of von Terzi (2021) but directly impacts ZFR is discussed in Section 4.2.

Table 1
Technical Specifications of the Radars Utilized During TRIPEx-Pol at JOYCE-CF

Specifications	X-band	Ka-band	W-band
Frequency (GHz)	9.4	35.5	94.0
Pulse repetition (kHz)	10	5.0	2.2–12.8
Number of spectral bins	4,096	512	128–512
Number of spectral average	10	19	11–13
3 dB beam width (°)	1.0	0.6	0.5
Nyquist velocity ($\pm ms^{-1}$)	80	10.5	1.8–10.2
Sensitivity at 1,560 m (dBz), 2 s integration	−40.7	−54.0	−51.1
Sensitivity at 1,168 m (dBz), 2 s integration	−43.9	−56.6	−53.8
Range resolution (m)	36	36	36
Temporal sampling (s)	2	2	3
Lowest clutter-free range (m)	300	400	300
Polarimetry	No	LDR	No

Note. The radars operate with frequencies in the X-, Ka-, and W-band and are all vertically pointing. Sensitivities are given at average heights of the ML top (1,560 m) and bottom (1,168 m).

The corrected data set has been used and described before by Mróz et al. (2021), who also studied ML processes on a single day from the campaign, and Vogel et al. (2021), who applied a neural network to identify riming events on several selected days.

4. Methods

Before we start applying the ZFR approach, we have in a first step to reliably identify the top and bottom of the ML for all profiles (Section 4.1). In a second step, we correct for attenuation within the ML (Section 4.2). A remaining problem, which was already discussed in Drummond et al. (1996) and Section 2 is the influence of vertical wind w on the ZFR. Using Doppler spectral signatures, we derive w for a subset of our profiles and test how much our statistical results of ZFR change when taking into account the influence of w (Section 4.3). In Section 4.4, we categorize each profile whether the snow entering the ML is rimed using a new method presented in Li et al. (2020) based on the dual wavelength ratio (DWR) between X and Ka-band ($DWR_{X,Ka}$) and MDV.

4.1. Detecting the ML Boundaries

Numerous approaches have been used to define the ML top and bottom. Early studies used the absolute values, gradients, or curvature of Ze (Drummond et al., 1996; Fabry & Zawadzki, 1995; Klaassen, 1988) or MDV (Klaassen, 1988; Zrnic et al., 1994). Baldini and Gorgucci (2006) summarized previously established methods and added the ML detection based on the standard deviation of polarimetric variables (differential reflectivity and differential phase shift). Also absolute values (Devisetty et al., 2019) and gradients (Bandera et al., 1998) of the linear depolarization ratio:

$$\mathrm{LDR} = \frac{Ze_{hv}}{Ze_{hh}} \tag{14}$$

have been used. Here, Ze_{hv} (in mm^6m^{-3}) is the reflectivity detected in the cross-polarized (vertical) channel after emission in the horizontal polarization. Ze_{hh} is the reflectivity received in the horizontal polarisation, in which the radiation was also emitted. LDR is large for particles in the early and intermediate melting stage, which are still large in size (compared to the fully melted particles), but already have increased Ze_{hv} due to the presence of liquid, which increases the dielectric factor.

We use the inflection points (points of maximum curvature) above and below the maximum LDR_{Ka} to infer the ML boundaries (Figure 2a). We think that these points characterize the boundaries of the ML well because they

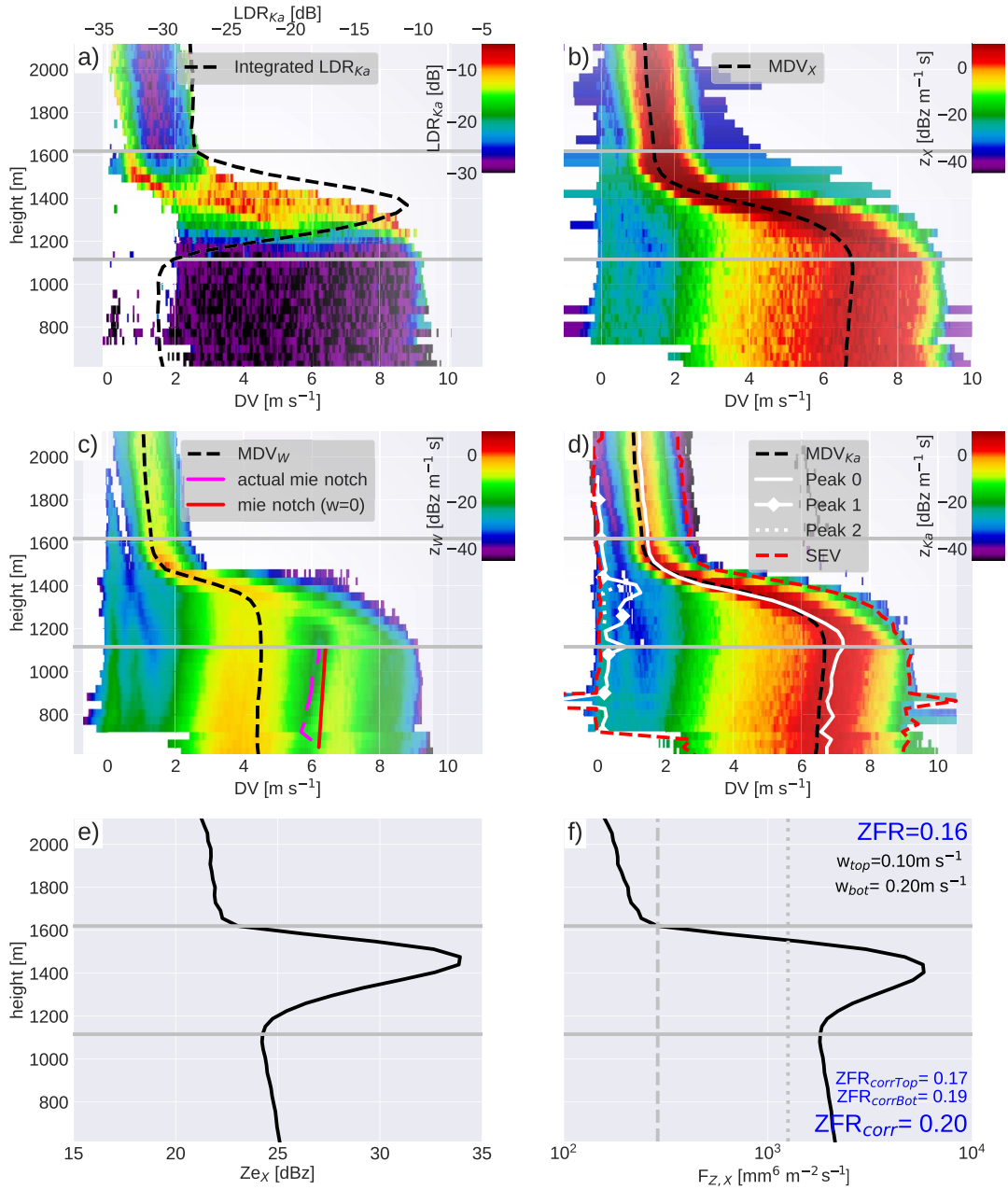

Figure 2. Spectra and profiles of integrated quantities from the 13 January 2019 07:25 UTC illustrating our melting layer (ML) detection, calculation of reflectivity flux ratio (ZFR), and corrections based on vertical wind estimate. (a) Spectral and integrated LDR$_{Ka}$; (b–d) Spectrogram and mean Doppler velocity of the X- (b), W- (c), and Ka-band (d); (e) Ze_X; and (f) F_Z. Panel (c) also shows the actual Mie-notch Doppler velocity (DV) and the one expected for $w = 0$ m s^{-1}; panel (d) also indicates the DV of the main peak and the peaks with slower DV; panel (f) includes also the estimate of w at the ML top derived from the peaks in panel (e) and at ML bottom derived from the Mie-notch in panel (d). Finally, also ZFR corrected by w$_{bot}$ (ZFR$_{corrTop}$), w$_{top}$ (ZFR$_{corrBot}$), and both w$_{top}$ and w$_{bot}$ (ZFR$_{corr}$) is shown in panel (f). LDR$_{Ka}$ of melting particles are up to 20 dB larger than the minimum observable LDR$_{Ka}$ visible in the rain part.

mark the region of a large change in the LDR gradient, expected when particles start to get wet (ML top) and when the shape of the particles collapse (ML bottom). The main advantage of this method is that the curvature of LDR$_{Ka}$ is relatively independent of the growth/shrinking processes of interest and mainly dependent on the degree of melting. In contrast, if the ML detection is based on Ze curvature, strong aggregation above the ML might cause a false ML top detection. Another advantage of using the inflection points is that they are independent of the absolute LDR values, which can be biased by miscalibration.

Although the use of the inflection points of LDR_{Ka} has advantages over other methods for detecting the ML boundaries, the determination of the inflection points and their connection to the ML boundaries must still be done carefully to detect only the heights associated with the ML boundaries. As many inflection points might be present in noisy profiles, we apply a temporal moving average of 5 min on LDR_{Ka}. Second, local maxima, and thus local inflection points, can also be caused by prolate ice particles, such as needles growing at about −6°C (Li et al., 2021, and references therein). Therefore, we disregard maxima, and corresponding inflection points, at temperatures below −1°C. Finally, we want to make sure that we exclude melting particles at the diagnosed ML top ($h_{melt,top}$) and ML bottom ($h_{melt,bottom}$). Since LDR_{Ka} increases already slightly above the height of the upper inflection point and decreases still slightly below the height of the lower inflection point, these points might be partly within the ML. Therefore, $h_{melt,top}$ (and $h_{melt,bottom}$) are chosen as the heights of the inflection points plus (minus) 36 m (equivalent to the height of one range gate).

Figure 2 shows qualitatively that our approach leads to similar heights of ML boundaries as previous approaches. The ML top is close to the maximum gradient of Ze (Figure 2e). Moreover, the ML bottom is close to the height, where the MDV reaches its maximum (Figure 2b). Furthermore, the spectral LDR reveals just above the ML small and slow particles with slightly enhanced LDR (up to −15 dB) typical for columnar or needle ice crystals (Li et al., 2021; Matrosov, 1991; Matrosov et al., 1996; Oue et al., 2015). From 1,600 m toward the ground, the LDR increases rapidly across all velocity bins while the smaller and slower ice particles appear to melt fastest.

4.2. Attenuation Caused by Particles in the Melting Layer

In general, the attenuation caused by melting particles is particularly important because the specific attenuation coefficient α (dB km^{-1}) is much higher within the ML than in rain for the same precipitation rate. It can have a non-negligible effect even at relatively low frequencies such as X-band (Bellon et al., 1997; Matrosov, 2008). To estimate and correct for the effect of attenuation within the ML we use the relation between the two-way attenuation A and the rain rate R at X-band provided by Matrosov (2008):

$$A[dB] = 0.048\, R\left[mm\, h^{-1}\right]^{1.05} \tag{15}$$

Since the rain rate at the bottom of the ML is not directly observed, we estimate it from the relation between Ze and R for stratiform rain given by Marshall et al. (1947):

$$Ze\left[mm^6 m^{-3}\right] = 200\, R\left[mm\, h^{-1}\right]^{1.6} \tag{16}$$

Neglecting very small reflectivity fluxes ($F_{Z,rain} < 30$ mm^6 m^{-2} s^{-1}), we find a median (90th percentile) R of 0.78 mm h^{-1} (1.45 mm h^{-1}). Those low R should cause a two-way attenuation in the ML aloft according to Equation 15 of only 0.04 dB (0.07 dB) or less than 1% (2%) difference between the unattenuated and the attenuated Ze in units of mm^6m^{-3}. Nevertheless, we apply the correction of attenuation in the calculation of ZFR.

4.3. Estimating Vertical Wind at ML Top and Bottom

Radar Doppler spectral methods for deriving w rely on the identification of spectral features whose fall velocity is well known. Any deviation of the measured Doppler velocity (DV) can then be assigned to vertical air motion. In mixed-phase clouds, the spectral peak of supercooled cloud droplets is commonly used as a tracer for w (Battan, 1964; Luke & Kollias, 2013; Zhu et al., 2021). Cloud droplets can be assumed to have negligible fall velocity and hence their spectral peak should be close to 0 m s^{-1} DV for $w = 0$ m s^{-1}. Due to the rapid increase of fall velocity of ice crystals even at small sizes, the cloud liquid peak is usually well separated from the ice and snow peak in the spectrum (e.g., in Figures 2b–2d). The technique is often limited by two factors: First, the sensitivity of the radar to small liquid drops increases with higher frequencies. However, as attenuation also increases with frequency, rain and the ML might severely attenuate the signal causing the liquid peak to be undetectable (second factor). In this study, we therefore decided to use the Ka-band spectra to identify the liquid peak as it provides a good compromise between sensitivity and attenuation.

To identify the peaks, a fourth-degree polynomial is fitted to the spectrum. Each local maximum is recognized as a peak, and the DV and Ze of the peak are calculated. The main peak (Peak-0), identified as the peak with

the largest reflectivity, follows the MDV closely. The DVs of the other peaks are mostly smaller than 1 m s^{-1} (Figure 2d). These peaks with smaller DV could be caused by cloud droplets, drizzle (Kollias et al., 2007), ice phase particles created by nucleation at warmer temperatures or secondary ice production (Li et al., 2021), or noise speckles in the spectrum. To identify the cloud droplet peaks, we apply a rather simple criterion based on the integrated reflectivity of the peaks and the DV of the peaks (in the case of more than two peaks). Only peaks with Ze between −50 and −30 dBz are taken into account. The lower reflectivity limit is chosen to disregard spurious peaks in the noise floor, the upper limit to disregard drizzle and ice-phase peaks. Compared to previous studies, we chose a relatively conservative upper limit for Ze. For example, Radenz et al. (2019) uses a threshold of −20 dBz, which is 10 dB higher. If there is more than one additional peak, we assign the peak with the smallest DV to the supercooled cloud droplets. Besides more sophisticated techniques that also use higher radar moments (e.g., Zhu et al., 2021), this DV-based separation has been widely used (Kalesse et al., 2016; Radenz et al., 2019) and takes advantage of the fact that even relatively small ice particles have considerable velocity (e.g., about 0.4 m s^{-1} at 200 µm according to Locatelli and Hobbs (1974)). After the cloud droplet peak is identified, the deviation of DV of this peak from 0 m s^{-1} is taken as an estimate of w at the ML top. In the example profile (Figure 2) w_{top} is 0.10 m s^{-1}, which is according to our convention a slight downdraft (w toward the ground). Considering this downdraft in the calculation of ZFR shifts it to a slightly larger value (from 0.16 to 0.17). In the absence of a cloud liquid peak, the lower spectral edge velocity *SEV* (Figure 2d) could be used to estimate w, too. We defined the *SEV*s as the smallest and largest velocities, where Ze exceeds the noise level by 3 dB. However, using *SEV* as an estimate might underestimate w since the cloud droplet peak could be broadened by turbulence.

In rain, a separated cloud liquid peak is usually not detectable in the Doppler spectra. However, differential scattering signatures, which can be attributed to a certain drop size, can be used to derive w (Kollias et al., 2002). These signatures have, for example, been used in size distribution retrievals (Tridon & Battaglia, 2015). More precisely, the backscattering cross-section of raindrops that are larger than the radar wavelength exhibit local minima ("Mie-notches") due to destructive interference (Kollias et al., 2002). At a frequency of 94.0 GHz (W-band), the first local minimum occurs for particles with a size of 1.67 mm, which corresponds to $v_t = 5.9$ m s^{-1} in standard conditions when applying the velocity size relation for raindrops of Atlas et al. (1973). When considering the effect of the air density on the particle velocity (Heymsfield et al., 2007) by multiplying $\left(\frac{p_0}{p}\right)^{0.54}$, where $p_0 = 1{,}013.25$ hPa is the standard pressure, the expected Mie-notch velocity for $w = 0$ m s^{-1} can be calculated for each height (Figure 2c). With decreasing pressure, the Mie-notch appears at higher velocities as the air density and hence also the air resistance decreases. Before identifying the local minima as the Mie-notch position, the spectra are averaged with a moving window over six DV bins (corresponds to 0.12 m s^{-1}). If the spectral reflectivity at the DV bin of the actual Mie-notch is smaller than −40 dBz, the profile is disregarded to avoid noisy signatures. Figure 2c nicely shows local minima in the observed spectrogram that are associated with this Mie-notch. Deviations of the observed DVs of these minima from the theoretically expected DVs directly show w (e.g., −0.20 m s^{-1} at the ML bottom). Taking w_{bottom} into account when calculating the ZFRs, shifts them (similar as the w correction at the ML top) to a slightly higher value (from 0.16 to 0.19).

4.4. Categorizing Profiles by Their Degree of Riming

Several studies show that fingerprints of riming can be detected in the MDV observed with vertically aligned Doppler radars, among other methods. Riming initially strongly increases the particle mass and, to a lesser extent, its size and cross-sectional area. As a result, v of rimed particles quickly exceeds that of unrimed particles and the degree of riming can be estimated from MDV_X (Kneifel & Moisseev, 2020; Mosimann, 1995). However, when particles fall with velocities smaller than 1.5 m s^{-1}, large unrimed snowflakes might be indistinguishable from small rimed crystals. As demonstrated by Mason et al. (2018) or Li et al. (2020), the addition of multi-frequency information can be used to improve the detection of riming, especially in this lower DV regime ($v < 1.5$ m s^{-1}). We make use of the separation into three categories (unrimed, transitional, rimed) presented by Li et al. (2020). They used ground-based in situ observations combined with collocated multi-frequency Doppler radar observations to derive the rime fraction for each profile and fitted a dual-wavelength ratio $DWR_{X,Ka}$-MDV_X relation which separates the observed profiles well into unrimed, transitional and rimed ice particles. Li et al. (2020) provide these fits for several ranges of precipitation rates, which are overall relatively similar. We use the relations fitted to

precipitation rates between 1 and 4 mm h^{-1}, which is the typical range of rain rates observed during the TRIPEx-pol campaign when a ML could be detected:

$$\mathrm{DWR}_{X,Ka} = 0.6 \cdot \mathrm{MDV}^{7.3}_{X,\rho-corr} \tag{17}$$

separates unrimed from transitional profiles, and

$$\mathrm{DWR}_{X,Ka} = 0.75 \cdot \mathrm{MDV}^{2.85}_{X,\rho-Corr} \tag{18}$$

separates transitional from rimed profiles. In both equations (Equations 17 and 18), $\mathrm{MDV}_{X,\rho-Corr}$ is the air density corrected MDV of the X-band radar.

4.5. Application of the ZFR Method Including Filtering, Averaging and Riming Degree Categorization on a Case Study

The ZFR diagnostic strictly holds only if multiple conditions are fulfilled (Section 1). We discuss the condition of inhomogeneity and the categorization into different riming degrees on the example of the time range between 06:00 and 07:30 on 13 January 2019 (Figure 3). Inhomogeneities are evident in Ze (Figure 3b) in the form of slanted fallstreaks (e.g., around 06:17 UTC, periods of high reflectivity) or periods of low Ze (06:55 UTC). Both, the region of enhanced Ze associated with the fallstreaks and the period of low Ze appear slightly earlier at the ML top than at the ML bottom. As a result, ZFR goes first through a minimum/maximum in case of the fallstreak/period of low Ze, followed by a maximum/minimum. In these cases, the temporal average of 2 min already reduces the fluctuation due to the inhomogeneity to a great extent. These 2 min can be considered a typical time a particle with an average v of 2–3 m s^{-1} requires passing a 300–400 m thick ML. At the passage of slanted cloud boundaries and period of low Ze, a significant amount of hydrometeors and thus F_Z exist only at the ML top or bottom. In this scenario, ZFR also reaches extreme values (e.g., at 06:52 UTC) that are not due to growth or shrinking processes within the ML. Therefore, we introduce a filter, that removes low fluxes ($F_{Z,top} <$ 30 mm^6 m^{-2} s^{-1} or $F_{Z,bottom}/0.23 <$ 30 mm^6 m^{-2} s^{-1}). Figure 3f illustrates that the most extreme ZFRs are well removed by applying this filter.

The filtering of small fluxes also helps to disregard profiles where the particle type cannot be categorized confidently. Small fluxes are correlated with small mean particle sizes and thus low MDV_X and $\mathrm{DWR}_{X,Ka}$. $\mathrm{DWR}_{X,Ka}$ is very insensitive to particles smaller than 1 mm (Ori et al., 2020). MDV_X cannot be used to distinguish the riming degree if the particle size is smaller than 1 mm and its size cannot be estimated accurately. For example, a particle population with low $\mathrm{DWR}_{X,Ka}$ and MDV_X of about 1.5 m s^{-1} (e.g., in the time range between 06:00 and 06:10 UTC) could be composed of small rimed particles or larger but unrimed particles. Considering only the time ranges, with sufficiently high F_Z the shown case is dominated by the transitional category in the first 70 min before unrimed particles dominate in the last 20 min (Figure 3e), and ZFR is overall relatively close to zero.

5. Mean Profiles of Radar Variables for Unrimed and Rimed Profiles

The evolution of the particle populations during the melting process can be best observed when looking at average vertical profiles of various radar variables. Although our ability to directly assign certain radar features to specific microphysical processes is often limited due to the particles' complex changes in the scattering properties (see Section 2), characteristic values of, for example, Ze and Doppler velocities can help to rule out the presence of certain processes. For instance, we know that for shedding to occur, the particles need to exceed certain size limits that are related to a certain maximum MDV or *SEV*. In particular, we investigate similarities and differences in the vertical profiles for rimed and unrimed particles in this section.

To make the comparison independent of the actual ML depth, we normalize the height of each profile relative to the ML boundaries (h_{rel}) so that $h_{rel} = 0$ corresponds to the ML bottom and $h_{rel} = 1$ to the ML top. On average, the ML contained in our data set are 397 m thick with a standard deviation of 86 m.

As already discussed in Section 4.1, LDR is very sensitive to the onset of melting due to the rapid change of the refractive index from ice to liquid water. The differences in the LDR profiles for unrimed and rimed profiles shown in Figure 4a) are surprisingly small. The most noticeable difference is a larger LDR peak for

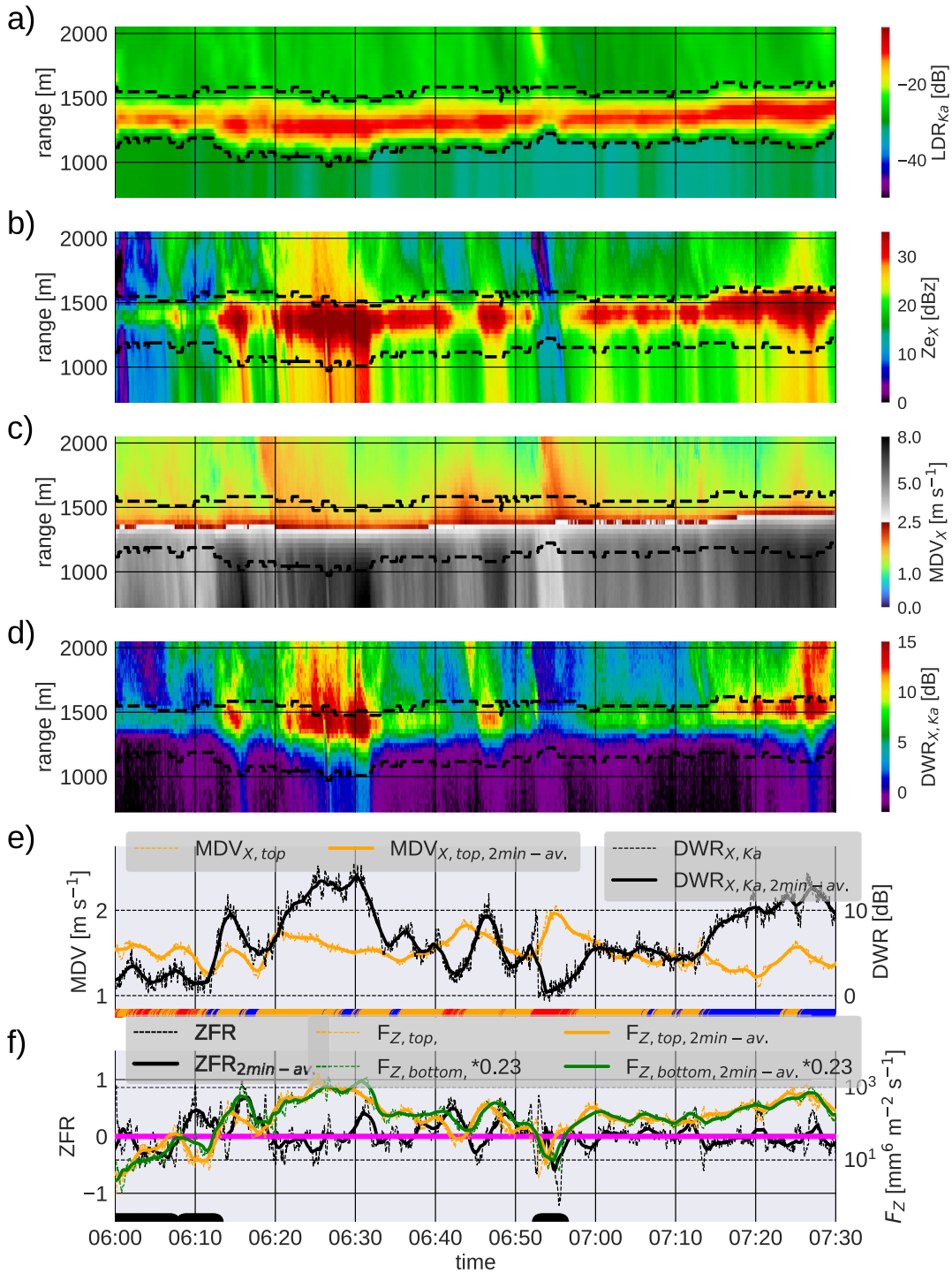

Figure 3. Radar variables and melting layer (ML) diagnostics from the morning hours of the 13 January 2019 illustrating the variability of the variables close to and within the ML, the categorization by the degree of riming, and challenges of the reflectivity flux ratio (ZFR) diagnostic. Time-height series: (a) LDR_{Ka}, (b) Ze_X, (c) MDV_X, and (d) $DWR_{X,Ka}$. In snow, positive $DWR_{X,Ka}$ indicate large particles; In rain, negative $DWR_{X,Ka}$ occur due to "super-Rayleigh scattering" (e.g., Mróz et al., 2020). Dashed lines mark the ML top and bottom. Timeseries of panel (e) MDV_X and $DWR_{X,Ka}$ at the ML top and riming degree categorization (bottom of the plot: blue: unrimed; orange: transitional; and red: rimed) (f) F_Z at the ML top and bottom, and ZFR. At the bottom of panel (f) all time ranges are marked by a black line where $F_{Z,top}$ is smaller than 30 mm^6 m^{-2} s^{-1} or $F_{Z,bottom}$·0.23 is smaller than 30 mm^6 m^{-2} s^{-1} (same as filter applied in Section 6). The magenta line in panel (f) marks ZFR = 0, which is to be expected under the melting-only assumption. Dashed lines show values on the original time grid and solid after applying a 2 min temporal average.

unrimed particles and a slight shift in peak position. While for unrimed particles, the LDR maximum is reached at $h_{rel} = 0.49$, it appears for the rimed and transitional category at a slightly lower height of $h_{rel} = 0.43$. This behavior is expected as the higher density of rimed particles should delay the melting process and hence cause the LDR maximum to occur lower in the ML.

While the evolution of the LDR is always a result of the changing structural particle properties (e.g., size and aspect ratio) and the altering refractive index, the v is mainly influenced by the change of the particle's cross-sectional area (if we assume the particle mass to be unchanged during melting). Based on laboratory experiments, Mitra et al. (1990) presented a relation with which the melting fraction f_{melt}, defined as

$$f_{melt} = \frac{m_{liq}}{m_{ice} + m_{liq}}, \tag{19}$$

can be derived from the relative increase in v of a single particle. m_{liq} is the liquid and m_{ice} the ice mass of the particle. Since radars observe the reflectivity-weighted v (the *MDV*) and not v of a single particle, we cannot estimate f_{melt} directly, but we can estimate the related reflectivity-weighted variable (cf. Equation 8):

$$f_{melt,Z} = \frac{1}{M^{(2)}} \int_0^\infty N(m)\, f_{melt}\, m^2\, dm \tag{20}$$

The $f_{melt,Z}$ is shown in Figure 4c (dashed lines) next to the MDV profiles of the two categories. The slightly slower increase of the melting process for rimed particles as indicated by LDR is also recognizable in $f_{melt,Z}$. According to the diagnosed $f_{melt,Z}$, 50% of the mass is liquid at $h_{rel} = 0.73$ ($h_{rel} = 0.67$) for unrimed (rimed), and 90% of the mass is melted at $h_{rel} = 0.49$ ($h_{rel} = 0.43$) for unrimed (rimed). The *SEV*s shown in Figure 4d reveal further details of the melting process. The lower *SEV* (left lines in Figure 4d) represents the melting of the smallest ice particles. From a h_{rel} of 0.5, the velocity is no further increasing indicating that the small particles melted already completely. There are also only slight differences between the unrimed and rimed categories regarding the evolution of the lower *SEV*. In contrast, the fastest and presumably also largest particles on the upper *SEV* (right lines) reach a similar saturation velocity only at the bottom of the ML. Similar to the LDR and MDV for the entire particle ensemble, the upper *SEV* also confirms the slower evolution of melting (increase in velocity) for the rimed category.

The average profiles of MDV and *SEV* are also useful for constraining the mean and maximum particle sizes in rain. We assume that vertical air motions which might shift the entire spectrum are randomly occurring in our data set and will therefore average out in our mean profiles. Turbulence will likely broaden the spectra and hence our size constraints represent an upper boundary of the true sizes. It should be noted that spectral multi-frequency retrievals have been developed which can also provide the full raindrop size distribution (Tridon & Battaglia, 2015; Tridon et al., 2013) but they haven't been applied to our entire data set yet.

The terminal velocity of raindrops can be mapped relatively unambiguously to raindrop size due to the well-defined particle shape (either sphere or oblate spheroid) (e.g., Atlas et al., 1973). At X-band we can assume that all raindrops are in the Rayleigh regime. We can thus use the MDV_X and *SEV* as a proxy for the mean and maximum drop size. Comparing the MDV_X at the ML bottom, we find 4.89 m s^{-1} for rimed and 5.42 m s^{-1} for unrimed profiles indicating slightly larger mean sizes for unrimed particles. Similarly, we can see from the upper spectral edge velocity *SEV* (right lines in Figure 4d) close to the ML bottom (8.21 m s^{-1} for unrimed and 7.72 m s^{-1} for rimed) that also the largest particles of the unrimed profiles have a larger mean mass than the largest particle of the rimed profiles.

These values of MDV_X and SEV indicate that there is most likely no hydrodynamic breakup in our data set. Hydrodynamic breakup occurs only for particles larger than 5 mm, which corresponds to terminal velocities of about 9 m s^{-1} at the average pressure at the ML bottom (923.4 hPa) (Pruppacher et al., 1998). Also shedding is most likely not relevant in this data set. Shedding occurs only for graupel and hailstones with a mass-equivalent size larger than about 8 mm, which corresponds to velocities of about 10 m s^{-1} once the particle is fully soaked and no air intrusions are left (Rasmussen et al., 1984). In contrast to these two processes, which are well known to be active mostly in convective systems where particle populations with large mean masses are present (Pruppacher et al., 1998), collisional breakup (Low & List, 1982; McFarquhar, 2004; Straub et al., 2010) cannot be ruled out even for the particle populations with smaller mean masses present in our data set.

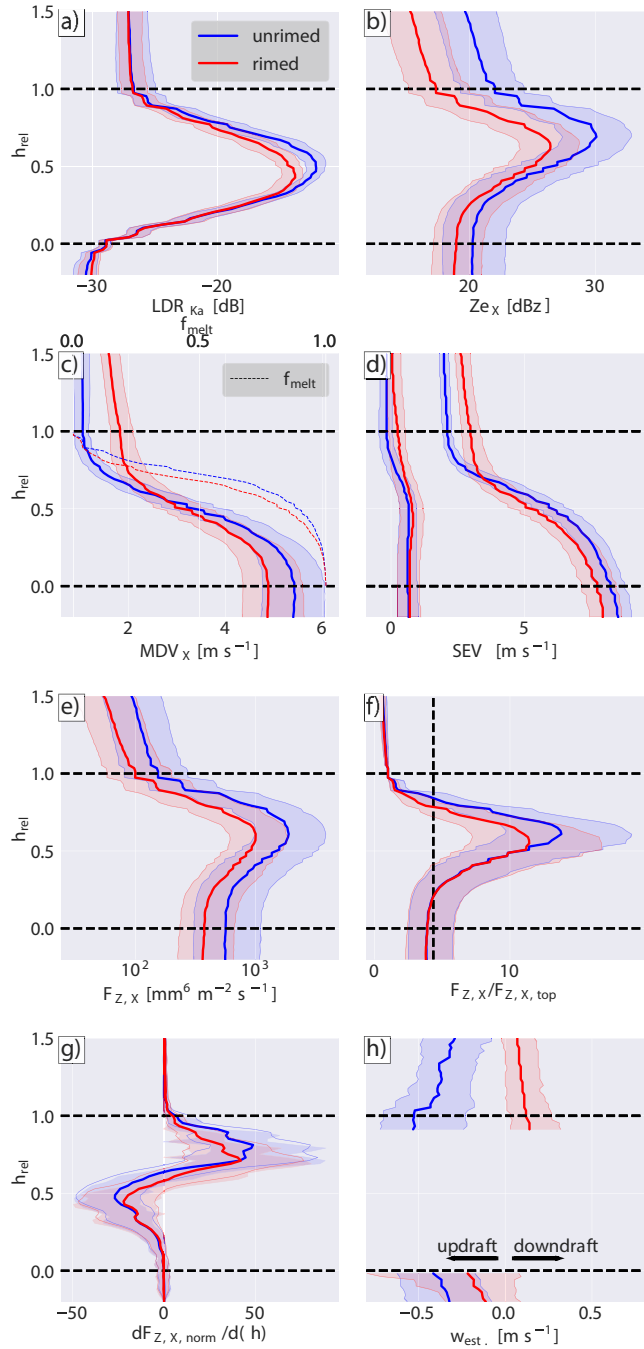

Figure 4. Profiles of the median (solid lines) and interquartile range (shading) of several variables in the melting layer (ML) indicating the melting degree, general properties of the particle population, and processes occurring within the ML. (a) LDR_{Ka}, (b) Ze_X, (c) MDV_X and $f_{melt,Z}$, (d) spectral edge velocities *SEV*, (e) F_Z, (f) F_Z normalized by $F_{Z,top}$ ($F_{Z,X,\mathrm{norm}}$), (g) the derivative of $F_{Z,X,\mathrm{norm}}$ ($dF_{Z,X,\mathrm{norm}}/d(-h)$), and (h) vertical wind w estimated from the spectral peaks for $h_{rel} > 1$ and from the Mie-notches for $h_{rel} < 0.0$. The height coordinate h_{rel} shows the relative position in the ML, where 0.0 corresponds to $h_{melt,bottom}$ and 1.0 to $h_{melt,top}$. $f_{melt,Z}$ in panel (c) is derived using Figure 2 from Mitra et al. (1990) as fitted by Frick et al. (2013). The vertical dashed line in panel (f) indicates ZFR = 0. Only profiles with $F_{Z,top} > 30$ $\mathrm{mm^6 m^{-2} s^{-1}}$ or $F_{Z,bottom} \cdot 0.23 > 30$ $\mathrm{mm^6 m^{-2} s^{-1}}$ are used to calculate medians and quantiles. Note that in only about 17% (41%) of the profiles the vertical wind at the ML top (bottom) can be estimated and thus the profiles in panel (h) are based on a smaller set of the data than panels (a–g).

As discussed in Figure 1, we expect that growth or shrinking processes will alter the F_Z profile. Most likely, multiple processes will act simultaneously and might compensate each other. The average profiles of F_Z are shown in Figure 4e revealing a shift of F_Z to larger values for unrimed profiles. For easier comparison of the two profiles, we normalize F_Z in Figure 4f by $F_{Z,top}$. The vertical dashed black line in Figure 4f indicates the value of the normalized F_Z ($F_{Z,X,\mathrm{norm}}$) at ML bottom that we would expect under the melting-only scenario. We find that unrimed and rimed profiles reach $F_{Z,X,\mathrm{norm}}$ at the ML bottom, which is slightly lower than the theoretical value for the melting-only scenario. This result implies that either no shrinking or growth processes are taking place in the ML at all, or that they compensate each other nearly perfectly. At least for profiles where aggregation above the ML is relevant, the first scenario seems rather unlikely as we know from previous in situ studies (Barthazy et al., 1998; Heymsfield et al., 2015; McFarquhar, 2004; Stewart et al., 1984; Willis & Heymsfield, 1989; Yokoyama et al., 1985) that aggregation is continuing in the upper part of the ML.

The pronounced peak and associated stronger vertical F_Z gradients (Figure 4g) for unrimed profiles fits into this interpretation. These stronger F_Z gradients could be explained by enhanced growth processes near the ML top (e.g., aggregation) and compensating shrinking processes in the lower part of the ML. The studies of Yokoyama et al. (1985) and Barthazy et al. (1998) also support this hypothesis. They observed size distributions and fall velocities of (mostly unrimed) particle populations in situ and derived number fluxes from which they concluded that aggregation and breakup are almost exactly balanced. Interestingly, for rimed profiles, these processes seem to be less pronounced. Similar to LDR_{Ka} and Ze, the rimed profiles reach the maximum in F_Z at lower relative heights. However, we need to interpret the F_Z inside the ML with care as the different morphology of unrimed and rimed particles might also influence their scattering properties during melting.

When we look at the F_Z profiles close to or just below the ML ($h_{rel} < 0$) in Figures 4e–4g changes in fall velocity and scattering properties are expected to be very small. In this region, we find very small changes of F_Z and its vertical gradient for unrimed and rimed profiles. If growth (e.g., condensation, collisional coalescence) or shrinking (e.g., collisional dissipation, evaporation) processes were dominant on average in the rain area directly below the ML, we would expect a stronger signal. This may indicate that the shrinking processes inside the ML, which compensate for growth processes aloft may be more related to melting particles (e.g., melt fragmentation) rather than raindrops.

The vertical wind at the ML top and bottom (Figure 4h) has been derived for a subset of the profiles which provide specific features (i.e., supercooled liquid peak in snow and Mie-notch in rain) in the Doppler spectra (Section 4.3). Those Mie-notch features in rain can only be found in 41% of the cases where F_Z is greater than 30 $\mathrm{mm^6\ m^{-2}\ s^{-1}}$. A supercooled liquid peak for estimating w at ML top is only found in 17% of the cases. For the unrimed profiles, a supercooled liquid peak is even rarer (only in about 2% of the data set filtered by low fluxes). This is expected because supercooled liquid droplets usually cause riming, which, if the riming is intense enough, causes the ice particles to fall into the rimed category. Despite the lower sample size, we can detect some interesting signatures in the derived w. At the ML bottom, we find updrafts which are slightly more intense for unrimed ($w = -0.41$ m s^{-1}) then for rimed ($w = -0.22$ m s^{-1}) profiles. At the ML top, the updraft for unrimed profiles is even more intense ($w = -0.53$ m s^{-1}) then at ML bottom. In contrast, for the rimed profiles, we find a slight downdraft ($w = 0.13$ m s^{-1}) at cloud top.

The observed vertical air motion features could be explained by both microphysical and thermodynamic processes. However, they could also be influenced by the sampling of the profiles. For synoptically driven stratiform clouds, the following three processes are likely to be most important. The formation of clouds and hydrometeor contents is usually related to the presence of large-scale updrafts (Lohmann et al., 2016). Clouds that show a Mie-notch related to larger raindrops or a supercooled liquid peak at the ML top might simply require enhanced w. Such a large-scale upward vertical motion would also well explain why we see a relatively continuous updraft at cloud top and bottom for unrimed profiles. The second source for vertical air motion is related to the diabatic cooling caused by melting of the particles which would induce downdrafts (Liu et al., 1997; Phillips et al., 2007). Other diabatic processes (e.g., riming, depositional growth) might lead to diabatic heating and thus updrafts. Lastly, variations in mass flux entering the ML can create convective cells (Szyrmer & Zawadzki, 1999). In these cells, periods of high mass flow correlate with downdrafts, and periods of low mass flow correlate with updrafts. We would assume that w from the last two mechanisms would occur much more randomly and on shorter time scales. Possibly, those fluctuations in w might then average out in the average profiles and be only included in the shaded area denoting the variability of observed w.

The question remains as to why we find slight downdrafts at the ML top for the rimed category. Besides the processes described above, the supercooled liquid peak used to estimate w might not be completely composed of small supercooled droplets with negligible terminal velocity but may also contain faster-falling drizzle. The presence of drizzle is also more likely for rimed profiles, as the collision efficiency of drizzle drops is strongly enhanced. Further, we expect drizzle to occur more frequently and with increasing sizes toward the ML (see also discussion in Kneifel and Moisseev (2020)). The presence of drizzle would cause the estimated w to shift to a slight downdraft similar to as we see it in Figure 4h.

Overall, a superposition of several effects (e.g., large-scale upward air motions and updrafts induced by diabatic heating) appear to be the most likely explanation for the observed vertical wind at ML top and bottom for most profiles. However, we have to keep in mind that this analysis might be biased simply because we might only be able to detect w in situations when an updraft is sufficient to maintain saturated conditions with respect to liquid water. In situations of stronger downdrafts, the supercooled liquid peak and potentially also the Mie-notch might be weaker or completely lacking.

6. Evaluation of the Melting-Only Assumption Using ZFR Statistics

In this section, we investigate whether the melting-only assumption is on average a valid assumption for our multi-month data set which is characterized by moderate hydrometeor contents and stratiform conditions (Section 5). To test the assumption, we analyze statistics of the ZFR separately for particle categories characterized by their riming degree (Section 4.4). To test the robustness of the methodology and the result, we apply different filters (Figures 5a–5c), apply temporal averaging (Figures 5d–5f) and correct profiles, where possible, for the vertical wind (Section 4.3, Figures 5g–5i).

Without applying any filter, the TRIPEx-pol data set provides 136.2 hr of ML observations, which divide into 32.9% unrimed, 20.1% transitional, and 47.0% rimed profiles (Figure 5a). Overall the median of ZFR is relatively close to zero (mostly slightly below zero) and the interquartile range (IQR) always covers ZFR = 0. Therefore, we can hypothesize that either the melting-only assumption is met and processes other than melting do not substantially modify F_Z or that two or more processes strongly compensate each other regardless of whether particles are rimed or unrimed.

The scatter of ZFR (visible by the IQR and the whiskers) narrows down strongly after we filter out low fluxes (flux filter F1; Figure 5b). By applying this filter, we focus our analysis on the cases with more intense precipitation, where a relatively clear assignment of riming categories is also possible (Section 4.5). The flux filter removes about 70% of the profiles and changes the relative contribution of the riming categories. However, the median of ZFR stays very close to zero and only slight changes are observed. Filtering out profiles of low relative humidity with respect to liquid water (RH < 95%) to exclude a potential impact of sublimation and evaporation on the ZFRs does shift ZFR slightly to values even closer to zero. This suggests that in some cases sublimation or evaporation might be responsible for a slight reduction of F_Z. However, applying this filter removes about another half of the data (Figure 5c). In the following analysis, we use the flux filter F1 as it is necessary to remove spurious signals. Since it changes the statistics little when low humidity profiles are filtered, we do not apply this filter in the following to maintain a balance between the quality of the filtering and statistical robustness. No matter which filter or associated profile reduction is applied (Figures 5a–5c), the median ZFR is always found close to zero and the IQR covers ZFR = 0.

In our analysis, we calculate ZFR as the ratio of F_Z at the ML top and F_Z at the ML bottom taken from the same time. To be able to do this, we must assume homogeneity, which is, for example, not valid if fallstreaks are present (Section 4.5). The effect of fallstreaks on ZFR can be mitigated or even eliminated by averaging over time periods longer than the time it takes particles typically to pass through the ML. As we can see in Figures 5d–5f, applying different temporal averages of 1, 2, and 5 min has only a small impact on the ZFR distributions with median values slightly below zero for all particle types. It appears that the effect of inhomogeneities produces rather random fluctuations in the ZFR (with insignificant biases) that cannot be substantially reduced by longer averaging times.

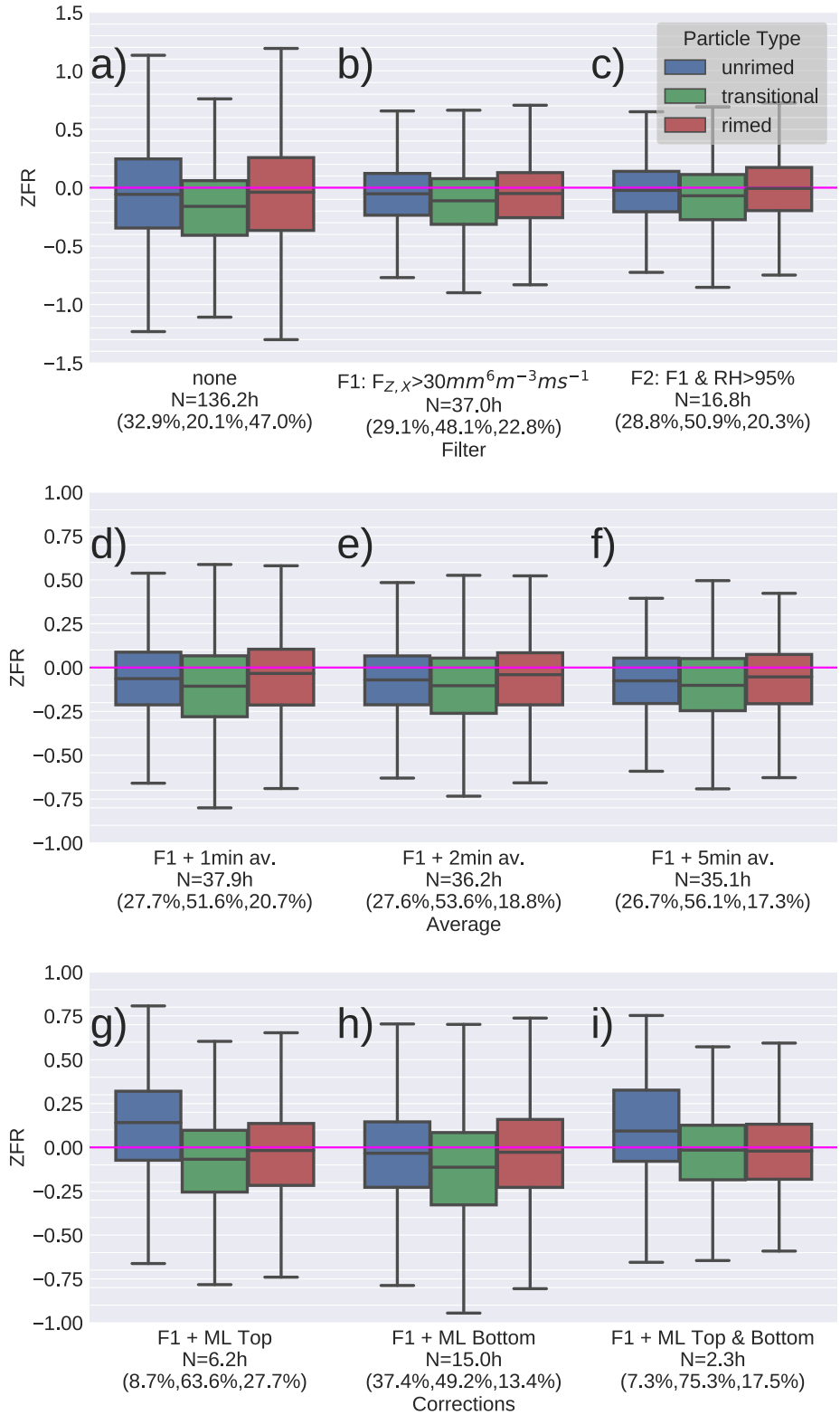

Figure 5. Boxplot of reflectivity flux ratio (ZFR) for different particle types (unrimed, transitional, and rimed) and different filters (first row, a–c), average periods (middle row, d–f) and corrections (last row, g–i). Each box shows the interquartile range of the distribution. The horizontal line within each box depicts the median. The whiskers show the rest of the distribution excluding outliers. Filters applied: F1: profiles with $F_{Z,top} < 30$ mm^6 m^{-2} s^{-1} or $F_{Z,bottom}\cdot 0.23 < 30$ mm^6 m^{-2} s^{-1} are removed. F2: in addition to Filter 1, profiles with relative humidity with respect to liquid water RH below 95% are removed. In panels (g–i) ZFR is corrected for w_{top} only in panel (g), w_{bottom} only in panel (h), and w_{top} and w_{bottom} in panel (i).

Correcting ZFR with w at the ML top and the ML bottom has only a slight effect on the statistics of transitional and rimed profiles which are now almost perfectly distributed around ZFR = 0 (Figure 5i). The reason for this small effect of the w correction might be related to the overall smaller w values found for rimed profiles (Figure 4h). As the average w at the ML top is downwards and upwards at ML bottom, the effects of correcting them for ZFR tend to cancel each other. This very close distribution of ZFR around zero for the rimed and transitional profiles corrected by w strengthens the original hypothesis of melting-only or particularly well-balanced effects (e.g., collisions and breakup). In contrast, for unrimed profiles, the correction with w estimated at the ML top (Figure 5g) shifts ZFR to values slightly above zero indicating that growth processes slightly dominate over shrinking processes. This fits with the observation of additional aggregation in the ML reported in previous studies (Barthazy et al., 1998; Heymsfield et al., 2015; McFarquhar, 2004; Stewart et al., 1984; Willis & Heymsfield, 1989; Yokoyama et al., 1985). Willis and Heymsfield (1989) has described that aggregation in the ML could be especially strong when comparatively larger particles enter the ML because these particles take longer to melt, allowing them to aggregate over a longer time than smaller particles.

Given the relatively strong effect of the w correction at ML top for unrimed profiles, we visually checked all spectra from the 23 different days where a supercooled liquid peak could be found. Overall, the supercooled droplet peak identification and related w estimate appears reasonable. One typical example is included in the appendix (Figure A1) which reveals the updraft at ML top and bottom. The updraft can visually also be seen as a slow-down or shift in the entire spectrogram toward smaller downward or even upward motions. This slow-down often also extends into the ML rather than being only located at the very top.

We also tested whether the smaller subset of profiles for which w could be derived might already have a systematically different statistic of the ZFRs even without applying the w correction. If we neglect the w correction, the statistics of the subset is similar to the larger set of profiles with no w correction applied (Figure 5b). The change in the distribution for unrimed profiles found in Figures 5g and 5i appears to be mainly driven by the w correction at the ML top. Unfortunately, we can estimate w at the ML top for unrimed profiles only in a small number of cases. Therefore, it remains an open question whether correcting w in all cases would shift the ZFR statistics of the entire data set or whether w is particularly high in the cases where w can be estimated from supercooled droplet peaks. To find indications of whether the subset of the profiles, where w can be determined for unrimed profiles (Figure 5g), have characteristic differences from the population of the entire F1 data set (after filtering with low fluxes; Figure 5b), we calculated percentiles of $\mathrm{DWR}_{X,Ka}$ at the ML top of these two groups. $\mathrm{DWR}_{X,Ka}$ is closely related to the mean size of aggregates. If one of the data sets had a significantly different mean size, the effect described by Willis and Heymsfield (1989) could make additional aggregation more likely for one data set than for the other. However, it turns out that $\mathrm{DWR}_{X,Ka}$ has similar median (90th percentile) for the entire filtered data set 8.71 dB (14.28 dB) and the subset 7.82 dB (13.01 dB). This suggests that the subset might be representative of the entire filtered data set.

From the various filters and tests applied we can conclude that the ZFR regardless of the category (unrimed, transitional, and rimed) is close to zero and the IQR always includes ZFR = 0. This means that either the melting-only assumption is met and processes other than melting do not substantially modify F_Z or that two or more processes compensate each other to a large extent. Only the correction of ZFR with w estimated at the ML top shifted ZFR from values slightly below zero to values slightly above zero. Whether this indicates that additional aggregation is masked on average by updrafts that cause a bias in ZFR, or whether rather the part of the data set where w can be estimated at the ML top shows particularly strong aggregation in the ML remains unclear. To answer this question, it is essential to obtain information about w in various weather condition, for example, by combining cloud radar observations with a radar wind profiler (Bühl et al., 2015).

7. Conclusions and Outlook

Globally, the majority of rainfall originates from melted ice particles. To accurately predict precipitation on the ground or to retrieve rainfall from space, a better understanding of the dominant microphysical processes that might occur in addition to melting in the ML are of key importance. Different radar remote sensing approaches and in situ observations have been used to infer those different processes. The ZFR approach proposed by Drummond et al. (1996) is both relatively simple and promising to infer the dominance of growth and shrinking processes in the ML. The relatively simple diagnostic is based on Ze and MDV measured with a low-frequency radar at ML

top and bottom. It allows assessing whether deviations from the melting-only scenario (every ice particle melts to a raindrop of the same mass) can be observed. Numerous previous studies documented differences in the melting behavior and associated microphysical processes for unrimed versus rimed ice particles entering the ML. In this study, we first used recently developed techniques (Li et al., 2020) to separate rimed, transitional and unrimed snow combining Doppler and multi-frequency information. This allowed us to study statistics of ZFR for the three particle categories based on 136 hr of ML observed by three collocated and vertically pointing Doppler radars (X-, Ka-, and W-band).

Known sources of uncertainty, such as vertical air motion, averaging time, or sub-saturated conditions, were assessed and their impact on the resulting ZFR statistics quantified. Similar to previous studies, we found that w can introduce significant biases in the ZFRs if not properly corrected. For a subset of the data that provided specific Doppler spectral features in rain and the ice part above the ML, we were able to derive the vertical air motion from the vertically pointing radar data.

The observed clouds and their particles are characterized by low to moderate hydrometeor contents and particle sizes, as shown by the mean values of Ze at the ML top and bottom and MDV_X at ML bottom. For these low to moderate particle sizes some processes (e.g., hydrodynamic breakup and shedding) can be excluded. These processes are more important in convective systems where large rimed particles are present (e.g., Bringi et al., 2020). Furthermore, the properties of the hydrometeor population, together with the relatively low values of the estimated w, indicate that mostly stratiform clouds were observed, which was to be expected for the observation period (November-February) in central Europe. Where possible to retrieve, w at ML top and bottom are mostly upwards. This might result from a superposition of several effects (e.g., synoptic-scale lifting and diabatic heating). Possible updrafts and downdrafts caused by diabatic cooling due to melting (Liu et al., 1997; Phillips et al., 2007), and additional circulations associated with this cooling effect (Szyrmer & Zawadzki, 1999), appeared to have a negligible effect on the mean profiles.

The large data set allowed us to derive robust ZFR statistics for different particle types. Considering all particle types together, the resulting median ZFR is only slightly lower than zero and the IQR includes zero. We interpret this result as evidence that the melting-only assumption is on average a valid assumption. After correcting slightly to strongly rimed profiles with w, the ZFR values which were initially below zero are shifted further to zero. Overall, tests with various filters or averaging time had the smallest effect on rimed and transitional profile categories. For unrimed profiles, ZFR is also slightly below zero as long as it has not been corrected with w at the ML top. However, after correction with w, ZFR shifts slightly to values above zero. A near-zero ZFR may indicate that no other microphysical process than melting substantially affects the hydrometeor population or that different processes compensate each other. The complete absence of additional growth or shrinking processes in the ML appears rather unlikely. The alternative interpretation of the near-zero ZFRs being caused by compensating processes, such as aggregation and breakup, is also in better agreement with previous in situ studies of Yokoyama et al. (1985) and Barthazy et al. (1998). ZFRs slightly below zero, as observed for rimed and transitional profiles, seem to indicate that shrinking processes slightly predominate over growth processes within the ML. In contrast, ZFRs slightly above zero, as observed for unrimed profiles when corrected with w at the ML top, suggest that growth processes, such as aggregation, slightly dominate over shrinking processes within the ML. This finding corroborates results in previous studies (Barthazy et al., 1998; Heymsfield et al., 2015; McFarquhar, 2004; Stewart et al., 1984; Willis & Heymsfield, 1989; Yokoyama et al., 1985) that found evidence that in profiles where aggregation above the ML is a relevant process, aggregation continues also within the ML.

Our results are overall in agreement with previous studies using the ZFR approach (Drummond et al., 1996; Gatlin et al., 2018; Mróz et al., 2021). The only previous statistical analysis of ZFRs by Gatlin et al. (2018) also indicated the general validity of the melting-only assumption. Profiles with increasing ML thickness showed a tendency for dominating growth processes, such as aggregation. Also, the case study analysis presented by Drummond et al. (1996) and Mróz et al. (2021) indicated a tendency for growth processes to dominate. Only for intense precipitation events and unrimed particles, breakup of large melting snowflakes can overtake the initial additional aggregation inside the ML. However, in all those previous studies, the impact of w was only estimated as an uncertainty range for ZFR if considered at all.

A particularly critical factor found in our analysis of the ZFR statistics is the estimation of w at the ML top, especially for unrimed profiles. For these profiles, w can only be estimated in about 2% of the data (after filtering

out low fluxes). Since the correction of w at the ML top shifts the ZFR from values slightly below zero to values slightly above zero, it would be particularly important to be able to estimate w at the ML top in more cases. Wind profiler observations (e.g., Bühl et al., 2015) can estimate w also in the absence of a supercooled droplet peak and thus in more cases and a larger height interval (e.g., also within the ML). Ideally, a wind profiler should be combined with a X-band profiling radar, as it can provide accurate estimates of ZFR since most particles still scatter in the Rayleigh regime at X-band. In addition, the X-band can also provide Doppler spectral information relevant for process studies while attenuation effects are still much smaller than at Ka- or W-band.

The main result of this study, that melting-only is a good assumption for clouds in the central European winter (which are mostly stratiform), may not be directly transferable to other climates and seasons where different cloud regimes (e.g., convective clouds) occur. If convective clouds constitute a significant portion of the observational data set, numerous different aspects could change the statistics. In these convective clouds, for example, larger ice particles occur, where shedding and hydrometeor breakup play a role and possibly shift ZFR to smaller values. In addition, convective clouds typically have significantly higher vertical velocities. This means that on the one hand processes like condensation/evaporation can play a larger role. On the other hand, this also makes it particularly necessary to correct ZFR for the vertical wind. Because of these expected differences, an analysis using similar procedures should be performed for radar data from other seasons and locations.

Obtaining a more complete picture of the ML processes is hampered by the limited knowledge of the relevant processes on the particle level, their significance, and the difficulty in interpreting radar observations of the ML. As with many other applications where information is gained for use in microphysical schemes, the main problem is that process rates cannot be derived directly from radar observations (Morrison et al., 2020). In our opinion, a closure between detailed modeling (where process rates are explicitly predicted), for example, with novel Lagrangian particle models like Brdar and Seifert (2018) and all observational fields (laboratory, in situ and remote sensing) is the most promising way forward. Colocated in situ observations of particle distributions and fall velocities can help answer the question of whether processes other than melting are important in the ML or whether these processes compensate for each other. These in situ observations could be made either by aircraft ascents and descents through the ML similar to Stewart et al. (1984); Willis and Heymsfield (1989); McFarquhar (2004); Heymsfield et al. (2015), preferably in conjunction with radar observations (Houze et al., 2017), or by ground-based observations at various altitudes along a mountain similar to Yokoyama et al. (1985) and Barthazy et al. (1998). If such in situ observations confirm the findings of Yokoyama et al. (1985) and Barthazy et al. (1998) that breakup must be considered even in cloud regimes where hydrodynamic breakup and shedding can be ruled out, the process rates for melting particle breakup should be quantified in laboratory studies and these processes should be considered in detailed microphysical schemes. To further advance the closure between model and observation, knowledge of the scattering properties of melting particles must also be improved. Better knowledge of scattering properties (e.g., the dielectric factor for melting particles of complex shape) could ease the interpretation of the radar observation and enable a more direct comparison with the models.

Appendix A: Example Doppler Spectra

Figure A1 shows a typical spectrogram that is classified as unrimed but shows a secondary peak. This secondary peak can be attributed to supercooled droplets (Section 4.3) and indicates an updraft of $w = -0.28$ m s^{-1} at the melting layer (ML) top. The Mie-notch feature in the rain part can be used to estimate w at the ML bottom, where also an updraft ($w = -0.34$ m s^{-1}) is present (Section 4.3). Interestingly, the Doppler velocity (DV) of the secondary peak increases continuously in and below the ML. While the peak is relatively narrow above the ML, the droplets presumably grow by collision-coalescence in and below the ML which increases their terminal velocity and broadens the spectral peak. Therefore, the DV of the secondary peak can no longer be used to determine w unless the fall velocity of the drops associated with that peak can be accurately estimated. Coincidentally, these two effects (non-negligible fall velocity and updraft) seem to balance almost exactly at the ML bottom, so that the peak of the secondary mode occurs almost exactly at 0 m s^{-1}.

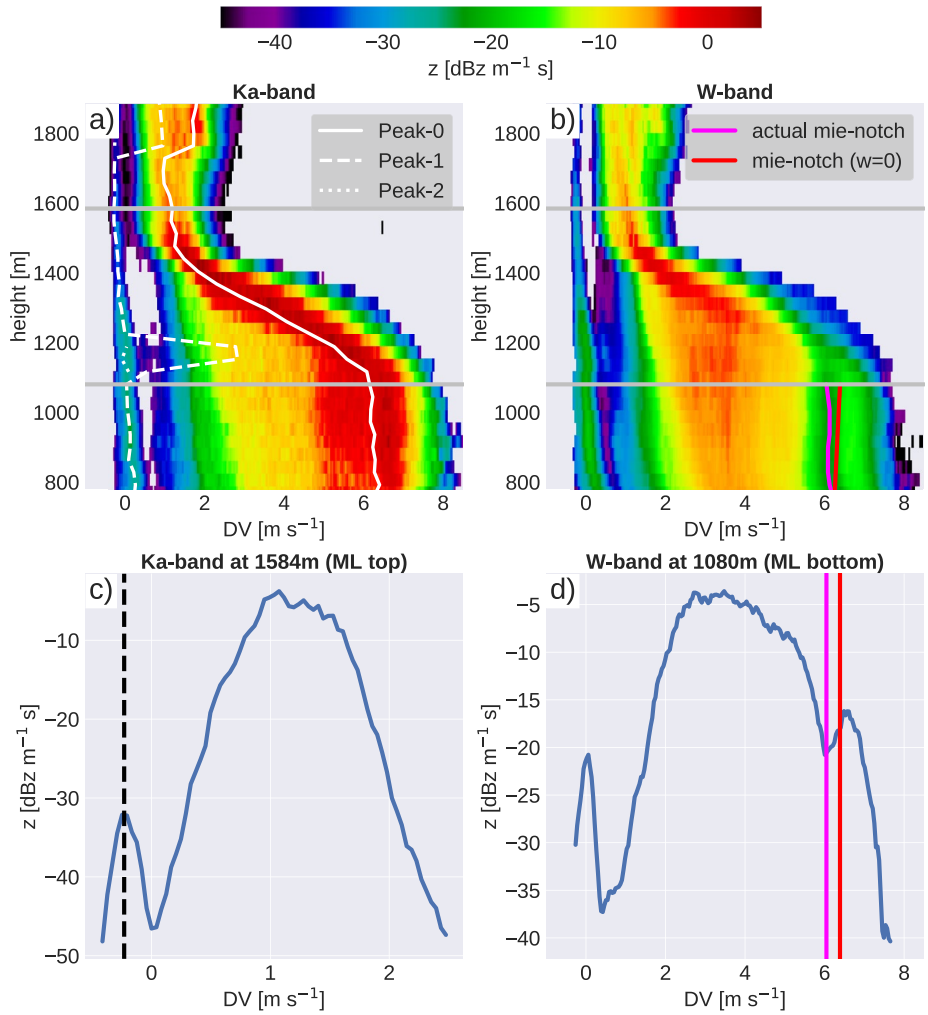

Figure A1. Spectrograms (a and b) and spectra (c and d) of the Ka-band (a and c) and W-band (b and d) from the 13 January 2019 06:18 UTC showing a typical case of an unrimed profile with updrafts at the melting layer (ML) top ($w = -0.28$ m s^{-1}) and the ML bottom ($w = -0.34$ m s^{-1}). The white lines in panel (a) show the Doppler velocity (DV) of the main, secondary, and third peaks. The magenta and red lines in panel (b) illustrate the actual Mie-notch DV and the one expected for $w = 0$ m s^{-1}. Doppler spectra at (c) the ML top and (d) the ML bottom (indicated by horizontal gray lines in panels (a and b) are depicted. Vertical lines indicate the DV of the secondary peak at ML top, the actual Mie-notch DV, and the one expected for $w = 0$ m s^{-1} at the ML bottom. Note that the peak around 0 m s^{-1} in panel (d) is most likely due to drizzle.

Acknowledgments
Contributions by M. Karrer, S. Kneifel, and J. Dias Neto were funded by the German Research Foundation (DFG) under grant KN 1112/2-1 and KN 1112/2-2 as part of the Emmy-Noether Group "Optimal combination of Polarimetric and Triple Frequency radar techniques for Improving Microphysical process understanding of cold clouds" (OPTIMIce). The TRIPEx-pol campaign and work provided by L. von Terzi have been supported by the DFG Priority Program SPP2115 "Fusion of Radar Polarimetry and Numerical Atmospheric Modelling Towards an Improved Understanding of Cloud and Precipitation Processes" (PROM) under grant PROM-IMPRINT (project number 408011764). The authors thank Davide Ori and Axel Seifert for the detailed discussion on the theory of the ZFR approach, flux conservation, and breakup processes implemented in state-of-the-art models. M. Karrer also acknowledges support from the Graduate School of Geosciences of the University of Cologne. Open access funding enabled and organized by Projekt DEAL.

Data Availability Statement

Code used for the data analysis and already processed data is freely available on GitHub: https://github.com/markuskarrer/ZFR_riming and Zenodo under https://doi.org/10.5281/zenodo.5959906. All data obtained at JOYCE-CF are freely available on request from http://cpex-lab.de/cpex-lab/EN/Home/JOYCE-CF/JOYCE-CF_node.html. The TRIPEx-pol data set is available at https://doi.org/10.5281/zenodo.6341509.

References

Atlas, D., Srivastava, R. C., & Sekhon, R. S. (1973). *Doppler radar characteristics of precipitation at vertical incidence* (Vol. 11, No. 1). https://doi.org/10.1029/RG011i001p00001

Baldini, L., & Gorgucci, E. (2006). Identification of the melting layer through dual-polarization radar measurements at vertical incidence. *Journal of Atmospheric and Oceanic Technology*, *23*(6), 829–839. https://doi.org/10.1175/JTECH1884.1

Bandera, J., Papatsoris, A. D., Watson, P. A., Tan, J., & Goddard, J. W. (1998). Method for detecting the extent of the melting layer. *Electronics Letters*, *34*(22), 2104–2105. https://doi.org/10.1049/el:19981462

Barthazy, E., Henrich, W., & Waldvogel, A. (1998). Size distribution of hydrometeors through the melting layer. *Atmospheric Research*, *47–48*, 193–208. https://doi.org/10.1016/S0169-8095(98)00065-9

Battan, L. J. (1964). Some observations of vertical velocities and precipitation sizes in a thunderstorm. *Journal of Applied Meteorology*, *3*(4), 415–420. https://doi.org/10.1175/1520-0450(1964)003<0415:soovva>2.0.co;2

Bellon, A., Zawadzki, I., & Fabry, F. (1997). Measurements of melting layer attenuation at X-band frequencies. *Radio Science*, *32*(3), 943–955. https://doi.org/10.1029/97RS00492

Brdar, S., & Seifert, A. (2018). McSnow: A Monte-Carlo particle model for riming and aggregation of ice particles in a multidimensional microphysical phase space. *Journal of Advances in Modeling Earth Systems*, *10*(1), 187–206. https://doi.org/10.1002/2017MS001167

Bringi, V., Seifert, A., Wu, W., Thurai, M., Huang, G. J., & Siewert, C. (2020). Hurricane Dorian outer rain band observations and 1D particle model simulations: A case study. *Atmosphere*, *11*(8), 879. https://doi.org/10.3390/ATMOS11080879

Bühl, J., Leinweber, R., Görsdorf, U., Radenz, M., Ansmann, A., & Lehmann, V. (2015). Combined vertical-velocity observations with Doppler lidar, cloud radar and wind profiler. *Atmospheric Measurement Techniques*, *8*(8), 3527–3536. https://doi.org/10.5194/amt-8-3527-2015

Cholette, M., Morrison, H., Milbrandt, J. A., & Thériault, J. M. (2019). Parameterization of the bulk liquid fraction on mixed-phase particles in the predicted particle properties (P3) Scheme: Description and idealized simulations. *Journal of the Atmospheric Sciences*, *76*(2), 561–582. https://doi.org/10.1175/JAS-D-18-0278.1

Devisetty, H. K., Jha, A. K., Das, S. K., Deshpande, S. M., Krishna, U. V., Kalekar, P. M., & Pandithurai, G. (2019). A case study on bright band transition from very light to heavy rain using simultaneous observations of collocated X- and Ka-band radars. *Journal of Earth System Science*, *128*(5), 136. https://doi.org/10.1007/s12040-019-1171-0

Drummond, F. J., Rogers, R. R., Cohn, S. A., Ecklund, W. L., Carter, D. A., & Wilson, J. S. (1996). A new look at the melting layer. *Journal of the Atmospheric Sciences*, *53*(5), 759–769. https://doi.org/10.1175/1520-0469(1996)053<0759:ANLATM>2.0.CO;2

Fabry, F. (2015). *Radar meteorology: Principles and practice*. https://doi.org/10.1017/CBO9781107707405

Fabry, F., & Zawadzki, I. (1995). Long-term radar observations of the melting layer of precipitation and their interpretation. *Journal of the Atmospheric Sciences*, *52*(7), 838–851. https://doi.org/10.1175/1520-0469(1995)052<0838:LTROOT>2.0.CO;2

Frick, C., Seifert, A., & Wernli, H. (2013). A bulk parametrization of melting snowflakes with explicit liquid water fraction for the COSMO model. *Geoscientific Model Development*, *6*(6), 1925–1939. https://doi.org/10.5194/gmd-6-1925-2013

Gatlin, P. N., Petersen, W. A., Knupp, K. R., & Carey, L. D. (2018). Observed response of the raindrop size distribution to changes in the melting layer. *Atmosphere*, *9*(8), 319. https://doi.org/10.3390/atmos9080319

Heymsfield, A. J., Bansemer, A., Poellot, M. R., & Wood, N. (2015). Observations of ice microphysics through the melting layer. *Journal of the Atmospheric Sciences*, *72*(8), 2902–2928. https://doi.org/10.1175/JAS-D-14-0363.1

Heymsfield, A. J., Bansemer, A., Theis, A., & Schmitt, C. (2021). Survival of snow in the melting layer: Relative humidity influence. *Journal of the Atmospheric Sciences*, *78*(6), 1823–1845. https://doi.org/10.1175/JAS-D-20-0353.1

Heymsfield, A. J., Bansemer, A., & Twohy, C. H. (2007). Refinements to ice particle mass dimensional and terminal velocity relationships for ice clouds. Part I: Temperature dependence. *Journal of the Atmospheric Sciences*, *64*(4), 1047–1067. https://doi.org/10.1175/JAS3890.1

Heymsfield, A. J., Schmitt, C., Chen, C. C. J., Bansemer, A., Gettelman, A., Field, P. R., & Liu, C. (2020). Contributions of the liquid and ice phases to global surface precipitation: Observations and global climate modeling. *Journal of the Atmospheric Sciences*, *77*(8), 2629–2648. https://doi.org/10.1175/JAS-D-19-0352.1

Hogan, R. J., Honeyager, R., Tyynelä, J., & Kneifel, S. (2017). Calculating the millimetre-wave scattering phase function of snowflakes using the self-similar Rayleigh–Gans Approximation. *Quarterly Journal of the Royal Meteorological Society*, *143*(703), 834–844. https://doi.org/10.1002/qj.2968

Houze, R. A., McMurdie, L. A., Petersen, W. A., Schwall Er, M. R., Baccus, W., Lundquist, J. D., et al. (2017). The Olympic Mountains Experiment (OLYMPEX). *Bulletin of the American Meteorological Society*, *98*(10), 2167–2188. https://doi.org/10.1175/BAMS-D-16-0182.1

Illingworth, A. J., Hogan, R. J., O'Connor, E. J., Bouniol, D., Brooks, M. E., Delanoë, J., et al. (2007). Cloudnet: Continuous evaluation of cloud profiles in seven operational models using ground-based observations. *Bulletin of the American Meteorological Society*, *88*(6), 883–898. https://doi.org/10.1175/BAMS-88-6-883

Kalesse, H., Szyrmer, W., Kneifel, S., Kollias, P., & Luke, E. (2016). Fingerprints of a riming event on cloud radar Doppler spectra: Observations and modeling. *Atmospheric Chemistry and Physics*, *16*(5), 2997–3012. https://doi.org/10.5194/acp-16-2997-2016

Kidd, C., Takayabu, Y. N., Skofronick-Jackson, G. M., Huffman, G. J., Braun, S. A., Kubota, T., & Turk, F. J. (2020). The global precipitation measurement (GPM) mission. *Advances in Global Change Research*, *67*, 3–23. https://doi.org/10.1007/978-3-030-24568-9_1

Klaassen, W. (1988). Radar observations and simulation of the melting layer of precipitation. *Journal of the Atmospheric Sciences*, *45*(24), 3741–3753. https://doi.org/10.1175/1520-0469(1988)045<3741:ROASOT>2.0.CO;2

Kneifel, S., & Moisseev, D. N. (2020). Long-term statistics of riming in nonconvective clouds derived from ground-based Doppler cloud radar observations. *Journal of the Atmospheric Sciences*, *77*(10), 3495–3508. https://doi.org/10.1175/JAS-D-20-0007.1

Knight, C. A. (1979). Observations of the morphology of melting snow. *Journal of the Atmospheric Sciences*, *36*(6), 1123–1130. https://doi.org/10.1175/1520-0469(1979)036<1123:OOTMOM>2.0.CO;2

Kollias, P., Albrecht, B. A., & Marks, F. (2002). Why mie? Accurate observations of vertical air velocities and raindrops using a cloud radar. *Bulletin of the American Meteorological Society*, *83*(10), 1471–1484. https://doi.org/10.1175/bams-83-10-1471

Kollias, P., Clothiaux, E. E., Miller, M. A., Albrecht, B. A., Stephens, G. L., & Ackerman, T. P. (2007). Millimeter-wavelength radars: New Frontier in atmospheric cloud and precipitation research. *Bulletin of the American Meteorological Society*, *88*(10), 1608–1624. https://doi.org/10.1175/BAMS-88-10-1608

Kumjian, M. R., Mishra, S., Giangrande, S. E., Toto, T., Ryzhkov, A. V., & Bansemer, A. (2016). Polarimetric radar and aircraft observations of saggy bright bands during MC3E. *Journal of Geophysical Research*, *121*(7), 3584–3607. https://doi.org/10.1002/2015JD024446

Leinonen, J., & von Lerber, A. (2018). Snowflake melting simulation using smoothed particle hydrodynamics. *Journal of Geophysical Research: Atmospheres*, *123*(3), 1811–1825. https://doi.org/10.1002/2017JD027909

Li, H., Möhler, O., Petäjä, T., & Moisseev, D. N. (2021). Multiyear statistics of columnar ice production in stratiform clouds over Hyytiälä, Finland. *Atmospheric Chemistry and Physics*, *21*(May), 1–26. Retrieved from https://acp.copernicus.org/preprints/acp-2021-332/

Li, H., Tiira, J., von Lerber, A., & Moisseev, D. N. (2020). Towards the connection between snow microphysics and melting layer: Insights from multi-frequency and dual-polarization radar observations during BAECC. *Atmospheric Chemistry and Physics*, *20*(15), 1–23. https://doi.org/10.5194/acp-2020-16

Liu, C., Moncrieff, M. W., & Zipser, E. J. (1997). Dynamical influence of microphysics in tropical squall lines: A numerical study. *Monthly Weather Review*, *125*(9), 2193–2210. https://doi.org/10.1175/1520-0493(1997)125<2193:DIOMIT>2.0.CO;2

Locatelli, J. D., & Hobbs, P. V. (1974). Fall speeds and masses of solid precipitation particles. *Journal of Geophysical Research*, *79*(15), 2185–2197. https://doi.org/10.1029/jc079i015p02185

Löffler-Mang, M., & Joss, J. (2000). An optical disdrometer for measuring size and velocity of hydrometeors. *Journal of Atmospheric and Oceanic Technology*, *17*(2), 130–139. https://doi.org/10.1175/1520-0426(2000)017<0130:AODFMS>2.0.CO;2

Lohmann, U., Lüönd, F., & Mahrt, F. (2016). *An introduction to clouds: From the microscale to climate*. Cambridge University Press. https://doi.org/10.1017/CBO9781139087513

Löhnert, U., Schween, J. H., Acquistapace, C., Ebell, K., Maahn, M., Barrera-Verdejo, M., et al. (2015). JOYCE: Jülich observatory for cloud evolution. *Bulletin of the American Meteorological Society*, *96*(7), 1157–1174. https://doi.org/10.1175/BAMS-D-14-00105.1

Low, T. B., & List, R. (1982). Collision, coalescence and breakup of raindrops. Part II: Parameterization and fragment size distributions. *Journal of the Atmospheric Sciences*, *39*(7), 1607–1618. https://doi.org/10.1175/1520-0469(1982)039<1607:ccabor>2.0.co;2

Luke, E. P., & Kollias, P. (2013). Separating cloud and drizzle radar moments during precipitation onset using Doppler spectra. *Journal of Atmospheric and Oceanic Technology*, *30*(8), 1656–1671. https://doi.org/10.1175/JTECH-D-11-00195.1

Marshall, J. S., Langille, R. C., & Palmer, W. M. K. (1947). Measurement of rainfall by radar. *Journal of Meteorology*, *4*(6), 186–192. https://doi.org/10.1175/1520-0469(1947)004<0186:morbr>2.0.co;2

Mason, S. L., Chiu, C. J., Hogan, R. J., Moisseev, D. N., & Kneifel, S. (2018). Retrievals of riming and snow density from vertically pointing Doppler radars. *Journal of Geophysical Research: Atmospheres*, *123*(24), 13807–13834. https://doi.org/10.1029/2018JD028603

Matrosov, S. Y. (1991). Theoretical study of radar polarization parameters obtained from cirrus clouds. *Journal of the Atmospheric Sciences*, *48*(8), 1062–1070. https://doi.org/10.1175/1520-0469(1991)048<1062:TSORPP>2.0.CO;2

Matrosov, S. Y. (2007). Modeling backscatter properties of snowfall at millimeter wavelengths. *Journal of the Atmospheric Sciences*, *64*(5), 1727–1736. https://doi.org/10.1175/JAS3904.1

Matrosov, S. Y. (2008). Assessment of radar signal attenuation caused by the melting hydrometeor layer. *IEEE Transactions on Geoscience and Remote Sensing*, *46*(4), 1039–1047. https://doi.org/10.1109/TGRS.2008.915757

Matrosov, S. Y., Reinking, R. F., Kropfli, R. A., & Bartram, B. W. (1996). Estimation of ice hydrometeor types and shapes from radar polarization measurements. *Journal of Atmospheric and Oceanic Technology*, *13*(1), 85–96. https://doi.org/10.1175/1520-0426(1996)013<0085:EOIHTA>2.0.CO;2

Matsuo, T., & Sasyo, Y. (1981a). Empirical formula for the melting rate of snowflakes. *Journal of the Meteorological Society of Japan. Series II*, *59*(1), 1–9. https://doi.org/10.2151/JMSJ1965.59.1_1

Matsuo, T., & Sasyo, Y. (1981b). Non-melting phenomena of snowflakes observed in subsaturated air below freezing level. *Journal of the Meteorological Society of Japan. Series II*, *59*(1), 26–32. https://doi.org/10.2151/JMSJ1965.59.1_26

Matsuo, T., Sasyo, Y., & Sato, Y. (1981). Relationship between types of precipitation on the ground and surface meteorological elements. *Journal of the Meteorological Society of Japan. Series II*, *59*(4), 462–476. https://doi.org/10.2151/JMSJ1965.59.4_462

McFarquhar, G. M. (2004). A new representation of collision-induced breakup of raindrops and its implications for the shapes of raindrop size distributions. *Journal of the Atmospheric Sciences*, *61*(7), 777–794. https://doi.org/10.1175/1520-0469(2004)061<0777:ANROCB>2.0.CO;2

Mitra, S. K., Vohl, O., Ahr, M., & Pruppacher, H. R. (1990). A wind tunnel and theoretical study of the melting behaviour of atmospheric ice particles. IV: Experiment and theory for snow flakes. *Journal of the Atmospheric Sciences*, *47*(5), 584–591. https://doi.org/10.1175/1520-0469(1990)047<0584:AWTATS>2.0.CO;2

Morrison, H., Thompson, G., & Tatarskii, V. (2009). Impact of cloud microphysics on the development of trailing stratiform precipitation in a simulated squall line: Comparison of one- and two-moment schemes. *Monthly Weather Review*, *137*(3), 991–1007. https://doi.org/10.1175/2008MWR2556.1

Morrison, H., van Lier-Walqui, M., Fridlind, A. M., Grabowski, W. W., Harrington, J. Y., Hoose, C., et al. (2020). Confronting the challenge of modeling cloud and precipitation microphysics. *Journal of Advances in Modeling Earth Systems*, *12*(8). https://doi.org/10.1029/2019MS001689

Mosimann, L. (1995). An improved method for determining the degree of snow crystal riming by vertical Doppler radar. *Atmospheric Research*, *37*(4), 305–323. https://doi.org/10.1016/0169-8095(94)00050-N

Mróz, K., Battaglia, A., Kneifel, S., D'Adderio, L. P., & Dias Neto, J. (2020). Triple-frequency Doppler retrieval of characteristic raindrop size. *Earth and Space Science*, *7*(3). https://doi.org/10.1029/2019EA000789

Mróz, K., Battaglia, A., Kneifel, S., Von Terzi, L., Karrer, M., & Ori, D. (2021). Linking rain into ice microphysics across the melting layer in stratiform rain: A closure study. *Atmospheric Measurement Techniques*, *14*(1), 511–529. https://doi.org/10.5194/AMT-14-511-2021

Myagkov, A., Kneifel, S., & Rose, T. (2020). Evaluation of the reflectivity calibration of W-band radars based on observations in rain. *Atmospheric Measurement Techniques*, *13*(11), 5799–5825. https://doi.org/10.5194/AMT-13-5799-2020

Neto, J. D., Kneifel, S., Ori, D., Trömel, S., Handwerker, J., Bohn, B., et al. (2019). The TRIple-frequency and Polarimetric radar Experiment for improving process observations of winter precipitation. *Earth System Science Data*, *11*(2), 845–863. https://doi.org/10.5194/essd-11-845-2019

Oraltay, R. G., & Hallett, J. (1989). Evaporation and melting of ice crystals: A laboratory study. *Atmospheric Research*, *24*(1–4), 169–189. https://doi.org/10.1016/0169-8095(89)90044-6

Oraltay, R. G., & Hallett, J. (2005). The melting layer: A laboratory investigation of ice particle melt and evaporation near 0°C. *Journal of Applied Meteorology*, *44*(2), 206–220. https://doi.org/10.1175/JAM2194.1

Ori, D., & Kneifel, S. (2018). Assessing the uncertainties of the discrete dipole approximation in case of melting ice particles. *Journal of Quantitative Spectroscopy and Radiative Transfer*, *217*, 396–406. https://doi.org/10.1016/j.jqsrt.2018.06.017

Ori, D., Schemann, V., Karrer, M., Dias Neto, J., von Terzi, L., Seifert, A., & Kneifel, S. (2020). Evaluation of ice particle growth in ICON using statistics of multi-frequency Doppler cloud radar observations. *Quarterly Journal of the Royal Meteorological Society*, *146*(733), 3830–3849. https://doi.org/10.1002/qj.3875

Oue, M., Kumjian, M. R., Lu, Y., Verlinde, J., Aydin, K., & Clothiaux, E. E. (2015). Linear depolarization ratios of columnar ice crystals in a deep precipitating system over the Arctic observed by zenith-pointing Ka-band Doppler radar. *Journal of Applied Meteorology and Climatology*, *54*(5), 1060–1068. https://doi.org/10.1175/JAMC-D-15-0012.1

Phillips, V. T., Pokrovsky, A., & Khain, A. (2007). The influence of time-dependent melting on the dynamics and precipitation production in maritime and continental storm clouds. *Journal of the Atmospheric Sciences*, *64*(2), 338–359. https://doi.org/10.1175/JAS3832.1

Pruppacher, H. R., Klett, J. D., & Wang, P. K. (1998). Microphysics of clouds and precipitation. *Aerosol Science and Technology*, *28*(4), 381–382. https://doi.org/10.1080/02786829808965531

Radenz, M., Bühl, J., Seifert, P., Griesche, H., & Engelmann, R. (2019). PeakTree: A framework for structure-preserving radar Doppler spectra analysis. *Atmospheric Measurement Techniques*, *12*(9), 4813–4828. https://doi.org/10.5194/AMT-12-4813-2019

Rasmussen, R. M., & Heymsfield, A. J. (1987). Melting and shedding of graupel and hail. Part I: Model physics. *Journal of the Atmospheric Sciences*, *44*(19), 2754–2763. https://doi.org/10.1175/1520-0469(1987)044<2754:masoga>2.0.co;2

Rasmussen, R. M., Levizzani, V., & Pruppacher, H. R. (1984). A wind tunnel and theoretical study of the melting behavior of atmospheric ice particles. III: Experiment and theory for spherical ice particles of radius <500 micrometers. *Journal of the Atmospheric Sciences*, *41*(3), 381–388. https://doi.org/10.1175/1520-0469(1984)041<0381:AWTATS>2.0.CO;2

Ryzhkov, A. V., & Zrnic, D. S. (2019). Polarimetric microphysical retrievals. In *Radar polarimetry for weather observations* (pp. 435–464). https://doi.org/10.1007/978-3-030-05093-1_11

Seifert, A., & Beheng, K. D. (2006). A two-moment cloud microphysics parameterization for mixed-phase clouds. Part 1: Model description. *Meteorology and Atmospheric Physics*, *92*(1–2), 45–66. https://doi.org/10.1007/s00703-005-0112-4

Stewart, R. E., Marwitz, J. D., Pace, J. C., & Carbone, R. E. (1984). Characteristics through the melting layer of stratiform clouds. *Journal of the Atmospheric Sciences*, *41*(22), 3227–3237. https://doi.org/10.1175/1520-0469(1984)041<3227:CTTMLO>2.0.CO;2

Straub, W., Beheng, K. D., Seifert, A., Schlottke, J., & Weigand, B. (2010). Numerical investigation of collision-induced breakup of raindrops. Part II: Parameterizations of coalescence efficiencies and fragment size distributions. *Journal of the Atmospheric Sciences*, *67*(3), 576–588. https://doi.org/10.1175/2009JAS3175.1

Szyrmer, W., & Zawadzki, I. (1999). Modeling of the melting layer. Part I: Dynamics and microphysics. *Journal of the Atmospheric Sciences*, *56*(20), 3573–3592. https://doi.org/10.1175/1520-0469(1999)056<3573:MOTMLP>2.0.CO;2

Thériault, J. M., & Stewart, R. E. (2010). A parameterization of the microphysical processes forming many types of winter precipitation. *Journal of the Atmospheric Sciences*, *67*(5), 1492–1508. https://doi.org/10.1175/2009JAS3224.1

Thompson, G., Field, P. R., Rasmussen, R. M., & Hall, W. D. (2008). Explicit forecasts of winter precipitation using an improved bulk microphysics scheme. Part II: Implementation of a new snow parameterization. *Monthly Weather Review*, *136*(12), 5095–5115. https://doi.org/10.1175/2008MWR2387.1

Tridon, F., & Battaglia, A. (2015). Dual-frequency radar Doppler spectral retrieval of rain drop size distributions and entangled dynamics variables. *Journal of Geophysical Research*, *120*(11), 5585–5601. https://doi.org/10.1002/2014JD023023

Tridon, F., Battaglia, A., & Kneifel, S. (2020). Estimating total attenuation using Rayleigh targets at cloud top: Applications in multilayer and mixed-phase clouds observed by ground-based multifrequency radars. *Atmospheric Measurement Techniques*, *13*(9), 5065–5085. https://doi.org/10.5194/AMT-13-5065-2020

Tridon, F., Battaglia, A., & Kollias, P. (2013). Disentangling Mie and attenuation effects in rain using a K_a-W dual-wavelength Doppler spectral ratio technique. *Geophysical Research Letters*, *40*(20), 5548–5552. https://doi.org/10.1002/2013GL057454

Vogel, T., Maahn, M., Kneifel, S., Schimmel, W., Moisseev, D. N., & Kalesse, H. (2021). Using artificial neural networks to predict riming from Doppler cloud radar observations. *Atmospheric Measurement Techniques*. Retrieved from https://amt.copernicus.org/preprints/amt-2021-137/

von Terzi, L. (2021). *TRIPEx-pol level-2 data*. Zenodo. https://doi.org/10.5281/ZENODO.5025636

Willis, P. T., & Heymsfield, A. J. (1989). Structure of the melting layer in mesoscale convective system stratiform precipitation. *Journal of the Atmospheric Sciences*, *46*(13), 2008–2025. https://doi.org/10.1175/1520-0469(1989)046<2008:SOTMLI>2.0.CO;2

Yokoyama, T., Tanaka, H., Akaeda, K., Ohtani, T., Yoshizawa, N., Yamanaka, M. D., et al. (1985). Observation on microphysical processes in the stratiform precipitations including melting layers at Mt. Fuji. *Journal of the Meteorological Society of Japan. Series II*, *63*(1), 100–111. https://doi.org/10.2151/jmsj1965.63.1_100

Zhu, Z., Kollias, P., Yang, F., & Luke, E. (2021). On the estimation of in-cloud vertical air motion using radar Doppler spectra. *Geophysical Research Letters*, *48*(1), e2020GL090682. https://doi.org/10.1029/2020GL090682

Zrnic, D. S., Raghavan, R., & Chandrasekar, V. (1994). Observations of copolar correlation coefficient through a bright band at vertical incidence. *Journal of Applied Meteorology*, *33*(1), 45–52. https://doi.org/10.1175/1520-0450(1994)033<0045:OOCCCT>2.0.CO;2